ABSTRACT

Title of thesis: **UNDERSTANDING FLAME STRUCTURE IN WILDFIRES USING LARGE EDDY SIMULATIONS**

Salman Verma, Master of Science, 2014

Thesis directed by: Professor Arnaud Trouvé
Department of Fire Protection Engineering

The structure of wildfire flames in the presence of crossflow was analyzed by utilizing suitable non-reacting numerical experiments with low speed flow over a hot isothermal horizontal semi-infinite surface. FireFOAM, a Large Eddy Simulation (LES) based solver developed by FM Global for fire protection engineering applications, was employed for all the calculations.

Early-time dynamics of Rayleigh-Taylor Instability (RTI) was first simulated using Direct Numerical Simulations (DNS) so that the solver could be verified against Linear Stability Theory (LST). Then attention was given to late-time dynamics in order understand the different stages (e.g., appearance of secondary instability, generation of larger scales due to interaction between structures) involved in the development of the instability.

The onset of thermal vortex instability, in a configuration with low speed flow over a hot isothermal semi-infinite horizontal plate, predicted using DNS was compared with the literature. Spatial evolution of various terms in the streamwise

vorticity equation was used to identify the dominant mechanisms responsible for the generation/evolution of vorticity. Streamwise evolution of the instabilities was studied and the effects of the changes in temperature and orientation of the plate on the thermal instabilities were also investigated.

Finally, a configuration with low speed flow over a hot isothermal semi-infinite horizontal strip was used to understand the effects of upstream Boundary Layer (BL) height and the length of the strip on both the thin horizontal and larger structures (analogous to Flame Towers (FT) observed in real wildfires and laboratory experiments).

UNDERSTANDING FLAME STRUCTURE IN WILDFIRES USING LARGE EDDY SIMULATIONS

by

Salman Verma

Thesis submitted to the Faculty of the Graduate School of the
University of Maryland, College Park in partial fulfillment
of the requirements for the degree of
Master of Science
2014

Advisory Committee:
Prof. Arnaud Trouvé, Chair and Advisor
Prof. André Marshall
Prof. Michael Gollner

Acknowledgements

I would like to thank my advisor Prof. Arnaud Trouvé for his support, patience and guidance throughout the program.

I would also like to thank Dr. Gollner and Dr. Marshall for their patience and support over the last few months.

Thanks also to all my present and former CFD group members: Andrew Voegele, Arthur Piquet, Ayodeji Ojofeitimi, Benoit Pouliquen, Chandan Kittur, Christine Pongratz, Christopher Briggs, Cong Zhang, James White, Maria Theodori, Mickael Durand, Sebastien Vilafayeau, Taylor Myers, Vivien Lecoustre, Xiaoyue Pi and Zohreh Ghorbani.

From the experimental side thanks to: Ajay Vikram Singh, Colin Miller, Daniel Gorham and Wei Tang.

Table of Contents

List of Acronyms

FT Flame Towers

RTI Rayleigh-Taylor Instability

KHI Kelvin-Helmholtz Instability

DNS Direct Numerical Simulations

LES Large Eddy Simulation

ILES Implicit Large Eddy Simulation

nLES Non-linear Large Eddy Simulation

SGS Sub-Grid Scale

RANS Reynolds Averaged Navier Stokes

LST Linear Stability Theory

LSTV Linear Stability Theory with Viscosity

LSTVMD Linear Stability Theory with Viscosity and Mass Diffusion

LSTVTD Linear Stability Theory with Viscosity and Thermal Diffusion

POD Proper Orthogonal Decomposition

DMD Dynamic Mode Decomposition

MDM Most Dangerous Mode

BL Boundary Layer

CVP Counter-rotating Vortex Pair

1: Introduction

1.1 Background and motivation

Wildland fire spread is often described as a function of three fire behaviour components; fuel, weather, and topography [1]. Since fire spread is essentially a series of ignitions, effects of fuels on spread are determined based on their propensity to ignite including loading, shape and size, compactness, continuity, and chemical content. The component that varies the most is the weather, changing both spatially and temporally, including atmospheric conditions such as temperature, relative humidity, stability, precipitation and wind speed. Whereas topography only changes in space, such as elevation, aspect, land features, and steepness of slope.

Finney et al. [2] recently called for the development of a fundamental theory for wildfire spread. Current operational models used for predictions of fire spread are either "empirically based" or "physically based". The latter class of models attempt to represent the physical processes, but lack a physical (or experimental) basis for the assumptions used to describe fuel particle ignition and fire spread. Although computational power has increased, numerical tools for both operational firefighting and long-term predictions continue to rely on semi-empirical fire spread models primarily developed in the early 1970's e.g., by Rothermel [3]. The lack of advancement in the fundamental understanding of fire spread renders the current

Figure 1.1: Flame zone structure viewed looking downwind (fire spreading away from camera) shows patches of instabilities soon after the fire starts when the longitudinal vortices have shorter wavelength. Taken from [4].

models unreliable. Without a fundamental theory for fire spread, combustion, fluid dynamics, and heat transfer processes cannot be reliably applied to develop a model that is truly "physically based" and consequently has a higher fidelity.

Haines ([5] and [6]) was the first to suggest (based on several observations) that horizontal vortices play a crucial role in wildfire spread. And recent studies of spreading wind-driven fires in a 3×3 [m] wind tunnel at the USDA Forest Service, Missoula Fire Science Laboratory showed coherent structures that formed in the streamwise direction of the flow (also referred to as longitudinal vortices [7]) as well as spanwise fluctuations that propagated to the downstream edge of the flame zone contributing to intermittent fuel heating [8], see Figure 1.1. The highly spatially-uniform fuel beds used in those experiments [4] allowed for a more repeatable observation of the structures than previous efforts. **The results suggested that flame spread in fine fuel beds is driven by non-steady convective heating**

Figure 1.2: Flame structure, viewed looking downwind, seen with stationary burners in [1].

and intermittent flame contact on fuel particles. These heating characteristics were measured using micro thermocouple arrays and high speed video. The displacement of the flaming region and the large experiment size, however, made it difficult to carefully study these properties.

In order to avoid these difficulties Gorham et al. [1,9] chose a stationary, non-spreading experimental fire configuration, as it allowed for a thorough statistical analysis of the flame structure. The investigations prior to Gorham were focused on time-averaged properties of the flame and not on the transient/intermittent effects, important in spread through fine fuels [8]. The instabilities in these experiments resembled those seen in spatially-uniform fuel beds (Figure 1.2). And the intermittent heating observed in the fuel bed experiments were observed with stationary burners as well. Overall, **the flame geometry/structure was shown to be an important factor for understanding fire spread.**

1.2 Approach

Non reacting cases were utilized in this study (to avoid complexities related to combustion, radiation etc.) for analyzing the instabilities seen in [1,4]. Beyond that high fidelity numerical approaches like DNS and LES were chosen, with the objective to develop a computational companion to the stationary burner experiments [1] and also with the hope that such a tightly coupled experimental/computational investigation will enhance our understanding of the flame structure in wildfires. Overall, this effort represents the starting point in a systematic investigation of the fluid/flame dynamics involved in wildfires.

The configurations chosen in this study are described below:

1.2.1 Configuration 1

RTI, which represents a buoyancy-driven unstable thermal mixing configuration without horizontal cross-flow, see Figure 1.3 (top). Essentially, in this configuration, a heavy (cold) fluid was placed on top of a light (hot) fluid and the interface was perturbed, and subsequently the growth of the perturbation was monitored. The purpose of these simulations was to assess the capability of the numerical solver, FireFOAM, by comparisons with LST in the early stages and to understand the physics involved in the growth of the instabilities in the later stages.

1.2.2 Configuration 2

Flow over a hot isothermal semi-infinite horizontal plate, outlined in Figure 1.3 (middle). This configuration is similar to the RTI configuration but there are two ad-

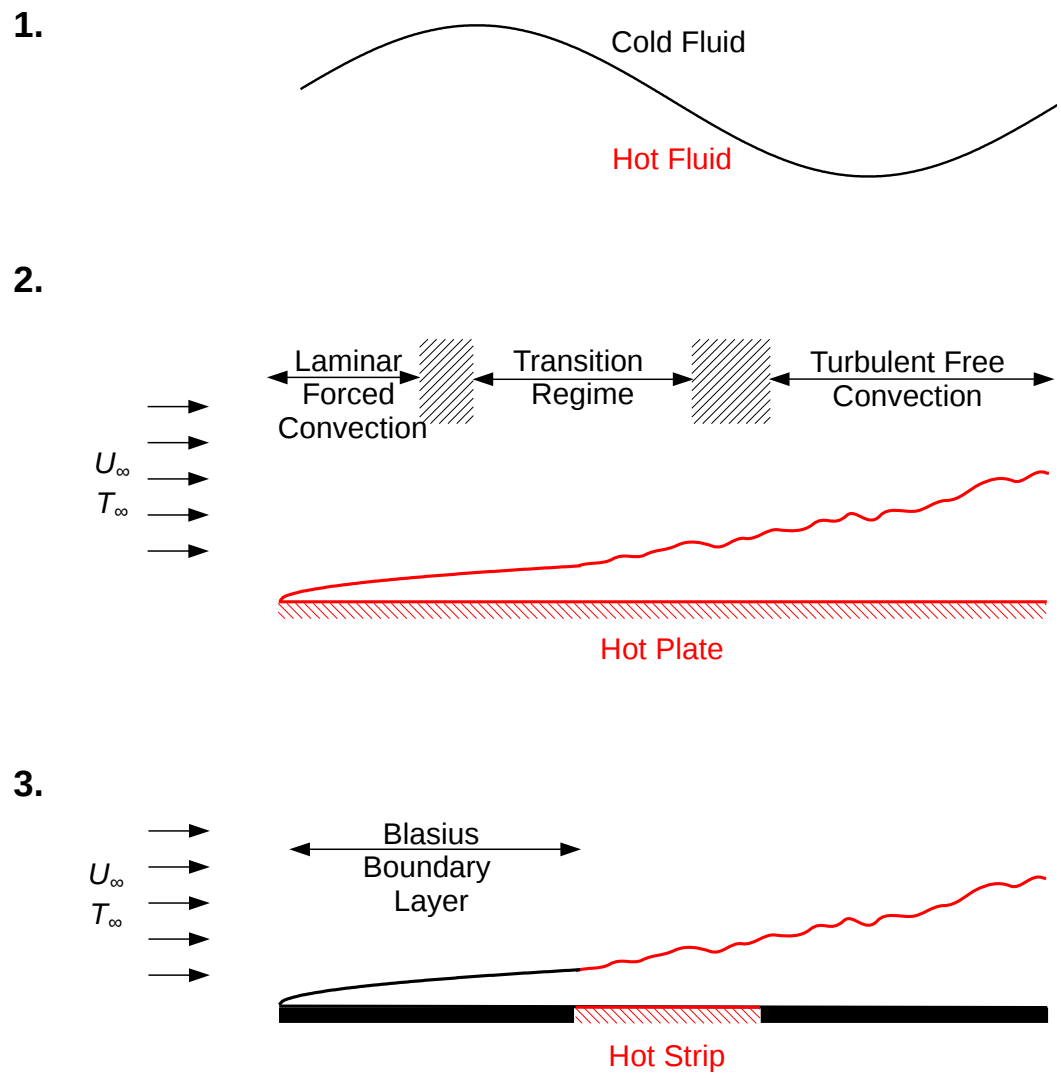

Figure 1.3: Non-reacting configurations utilized in the present study: RTI setup (1), flow over a hot isothermal semi-infinite horizontal plate (2), adapted from [7], and flow over a hot isothermal semi-infinite horizontal strip, representing a line source (3).

ditional elements; the cross-flow and heat transfer from the plate. DNS was carried out to see how well thermal instability onset location can be predicted numerically, since prior numerical studies in the literature had some issues e.g., assumption of two dimensionality, inadequate grid resolution. Streamwise evolution of various terms in the streamwise vorticity equation and also the evolution of the structures was analyzed. Effects of changes in the temperature of the hot surface and the plate orientation, on the thermal instability, were then studied in this setup.

1.2.3 Configuration 3

Same as above but with a strip of finite length in the streamwise direction, instead of a plate, presented in Figure 1.3 (bottom). This configuration was chosen to study the effects of the incoming BL height and the length of the heated region on the thermal instability.

1.3 Prior and related studies

1.3.1 Rayleigh-Taylor Instability (Configuration 1)

The literature for RTI, although vast, is not being discussed here, as no attempt was made in this study to answer any of the open questions related to RTI. It was just used as a tool to first verify the solver and then to enhance our understanding of the problem at hand.

But some of the necessary literature is presented in Chapter 3.

1.3.2 Low speed flow over a hot isothermal semi-infinite horizontal plate (Configuration 2)

Buoyancy effects in laminar forced convective flow over a heated horizontal semi-infinite flat plate were first studied by Mori [10]. However, only weak buoyancy forces were considered and hence no instabilities were involved. Sparrow and Minkowycz [11] studied independently the same problem but with a broader scope, by analyzing the buoyancy effects at various Pr, particularly because it was expected that these effects would be larger for low Pr fluids. They also corrected an error in the sign of the buoyancy term in Mori's analysis. Again, however, the study did not involve instabilities.

Hauptmann [12] obtained the same results by means of an approximate integral technique, whereas Mori [10] and Sparrow and Minkowycz [11] derived similarity equations which were integrated numerically. Some comments were made on BL stability as well but no conclusions were drawn due to the level of approximations involved in the procedure.

Redekopp and Charwat [13] evaluated the validity of the Boussinesq approximation, which neglects the effect of density variations on the inertial terms but retains the buoyant body force, invoked in [10–12]. No comments were made on the stability of the BL.

Wu and Cheng [14] were the first to theoretically come up with the conditions for the onset of thermal instability. However, the validity of their results was questioned in subsequent studies by Chen and Mucoglu [15] and Moutsogluo et al. [16].

At the same time, Moutsogluo et al.'s [16] predictions related to thermal instability onset were about two orders of magnitude lower than those in experiments by Gilpin et al. [17]. Yoo et al. [18] were able to use a more refined analytical technique to improve Moutsogluo et al.'s [16] results, however, the issue was apparently not settled [19]. Similar theoretical investigations still continue to appear in the literature [20,21], but they are also plagued e.g., by the assumption of two dimensionality and are limited to just the prediction of onset of instability. It is worth noting that even though these investigations are categorized as theoretical/analytical, they also require elaborate numerical procedures, see e.g., [21].

The studies by Imura et al. [7] and Gilpin et al. [17] were the first experimental investigations of this configuration. The parameter $\mathrm{Gr}_x/\mathrm{Re}_x^{3/2}$ (also suggested by Wu and Cheng [14], whereas Mori [10] and Sparrow et al. [11] used $\mathrm{Gr}_x/\mathrm{Re}_x^{5/2}$) was found to be of interest, with Re_x and Gr_x representing the local Reynolds and Grashof number, respectively, and defined as:

$$\mathrm{Re}_x = \frac{U_\infty x}{\nu} \tag{1.1}$$

and

$$\mathrm{Gr}_x = \frac{g\beta(T_w - T_\infty)x^3}{\nu^2} \tag{1.2}$$

where, x is the distance from the leading edge of the plate, U_∞ the freestream velocity, ν the kinematic viscosity, g acceleration due to gravity, β the volumetric thermal expansion coefficient and T_w (T_∞) the wall (freestream) temperature.

They were able to observe a first region of laminar forced convection near the leading edge ($\mathrm{Gr}_x/\mathrm{Re}_x^{3/2}<100$), followed by a second region featuring longitudinal

vortices and their growth to finite amplitude ($100<\mathrm{Gr}_x/\mathrm{Re}_x^{3/2}<300$) and finally a transition to a turbulent flow region ($\mathrm{Gr}_x/\mathrm{Re}_x^{3/2}>300$).

A heated flat plate was tested, by Wang [22], in a wind tunnel to study mixed convection in both upward and downward positions. The points of onset of instability caused by the buoyancy effect were examined and correlated in terms of the dimensionless groups.

Experimental results covering the transition vortex flow regime of mixed convection over a heated, horizontal flat plate were presented by Moherreri et al. [23]. That same year convective instability and buoyancy effects on forced convection heat transfer in horizontal boundary layers heated from below by a constant temperature plate were studied experimentally, by Cheng et al. [24], for flow regimes with $\mathrm{Re}_x = 2.5 \times 10^4$ to 2.2×10^6 and $\mathrm{Gr}_x = 2 \times 10^8$ to 1.5×10^{12}. Cheng et al. followed this study by another one [25] where they performed flow visualization experiments in a low-speed wind tunnel to study vortex instability of laminar natural convection flow along inclined isothermally heated plates having inclination angles from the horizontal of $\theta = 0$, 5, 10, 15 and 20 degrees.

Numerically, this configuration was investigated with Reynolds Averaged Navier Stokes (RANS) simulations by Ramachandran et al. [26]. The flowfield was resolved by solving two dimensional RANS equations and it was observed that such an approach was inherently inadequate. The inadequacies of assuming a two dimensional flowfield was attributed to its inability to reasonably capture the transition region which comprises the onset of longitudinal vortices and their eventual breakup into full turbulence [27].

As far as the use of a high fidelity tool like LES is concerned, the study by Ojofeitimi [27] seems to be the only one. Ojofeitimi showed a very good agreement with Gilpin et al's [17] experimental data in all three regimes (laminar forced convection, transition and turbulent free convection). However, an inadequate grid resolution close to the thermal instability location seems to have been used in that study, see Chapter 4 for a detailed discussion.

Overall, following comments can be made regarding the available literature on this flow configuration -

1. There seems to be sufficient experimental data for a quality validation of the flow solver in this configuration.

2. The use of a high fidelity tool like DNS or LES is limited to only one study [27], wherein, the grid resolution seems to be inadequate close to the thermal instability location.

3. It appears that pairing of the longitudinal vortices to give bigger structures has not been studied yet (theoretically/analytically or experimentally or numerically).

1.3.3 Low speed flow over a hot isothermal semi-infinite horizontal strip (Configuration 3)

Haines et al. [28] were the first to report visualizations of a horizontal Counter-rotating Vortex Pair (CVP) with axes in the downstream direction. A hot wire was used in one of their experiments. Similarly, Smith et al. [29] studied the effects of

a heated line source (a nichrome wire was used) on a Blasius BL. They did see a CVP however other than the smoke photographs, there was no documentation of the formation process of the longitudinal vortex pair from the transverse vorticity of the boundary layer. Effects of incoming BL were also not studied. Beyond that since they used a wire and not a strip (which is a more realistic representation of real fires) they could not investigate the effects of the streamwise length of the line source.

Heilman [30] and Heilman et al. [31] used a two dimensional model to simulate lines of extreme surface heating. Several qualitative conclusions were drawn but eventually the need for quality three dimensional simulations was stressed. It should be noted that the vortices involved in this study were not aligned with the freestream velocity, in other words, they were not longitudinal like those seen in [1, 4].

1.4 Research objectives

This study was aimed at:

1. Assessing/Verifying/Validating FireFOAM (OpenFOAM) and establishing the ability of LES to capture the instabilities (vortical structures) and flame wrinkling properties observed in experimental configurations.

2. Analyzing the structure of wildfire flames in the presence of crossflow by utilizing well designed non-reacting numerical experiments with flow over a hot isothermal semi-infinite horizontal surface.

3. Identifying the dominant mechanisms that lead to the generation/evolution of vorticity in wildfires (again using simple non-reacting cases).

4. Systematically investigating the effects of changing the temperature of the hot surface, the surface orientation, the upstream BL height and the streamwise length of the hot surface on the observed instabilities.

1.5 Contributions

- FireFOAM has been thoroughly verified/validated against LST for RTI, both in terms of the exponential perturbation growth and the Most Dangerous Mode (MDM).

- Different stages of RTI, have been simulated. It temporally takes the same course as the streaks take spatially in e.g., the stationary burners [1].

- First DNS for predicting the onset of thermal instability in Configuration 2 has been carried out.

- Spatial evolution of various terms in the streamwise vorticity equation has been analyzed to identify the dominant contributors towards the generation/evolution of streamwise vorticity in Configuration 2.

- Streamwise evolution of the instability in Configuration 2 has been qualitatively shown. Simulations suggest that flow fluctuations follow a natural evolution from high- to low-frequency/wavenumber (corresponding length scales grow in size) as one moves to downstream locations. There is no natural limit

to that evolution in Configuration 2.

- Effects of changes in the temperature and orientations of the plate on the instabilities have been qualitatively shown.

- In Configuration 3; the effects of changes in the upstream BL height and the streamwise length of the hot strip have been shown, again qualitatively. Simulations suggest that flow fluctuations follow again a natural evolution from high- to low-frequency/wavenumber (corresponding length scales grow in size) as one moves to downstream locations. There is now a natural limit to that evolution associated with the size of the strip.

1.6 Thesis outline

Details regarding the numerical tool i.e., FireFOAM (OpenFOAM) are discussed in Chapter 2, wherein a brief description of the governing equations is followed by some comments on LES. Then the filtered governing equations are discussed, after which the Sub-Grid Scale (SGS) turbulence modelling strategy is presented.

A discussion of RTI is presented in Chapter 3. First, equations for LST, Linear Stability Theory with Viscosity (LSTV), Linear Stability Theory with Viscosity and Mass Diffusion (LSTVMD) and Linear Stability Theory with Viscosity and Thermal Diffusion (LSTVTD), are provided. Then FireFOAM is thoroughly verified/validated in terms of, the perturbation growth with time (against LST) and the MDM (against LSTV and LSTVTD). This chapter ends with a discussion on the late-time dynamics and variation of horizontal length scales, with time, in

such configurations, which is pertinent to the generation of large vortical structures (towers) from thin horizontal (finger-like) structures.

Results from simulations of Configuration 2 are presented in Chapter 4. First, DNS is carried out to predict the onset of thermal instability. Then spatial variation of various terms in the vorticity equation is used to identify the dominant mechanisms that lead to the generation/evolution of vorticity in this configuration. The streamwise evolution of the instability is then discussed, after which the effects of variation in the plate temperature and orientation on the thermal instability are elucidated.

Results from simulations related to Configuration 3 are provided in Chapter 5. First, the thermal instability onset criteria issue is briefly discussed. As already mentioned this set-up was amenable for investigating the effects, of the upstream BL height and streamwise length of the hot region, on the dominant length scales.

In Chapter 6 the study is summarized, conclusions are drawn and future work is discussed.

2: FireFOAM (OpenFOAM)

FireFOAM [32, 33] is based on the OpenFOAM CFD library [34], which has attracted a lot of attention in recent past (both from the academia and the industry) due, primarily, to the following main features:

- Open access to its source code.
- Ease of its extensibility due to object oriented C++ [35], which is of paramount importance, especially, in a research environment as new models/solvers/boundary-conditions can be incorporated fairly easily.
- Availability of a number of advanced models for describing multi-physics flow problems (e.g., turbulence, combustion, multiple phases).
- Ability to handle polyhedral meshes, hence making the transition from canonical academic problems to practical devices fairly straighforward.
- Good scalability upto 1000s of processors.
- Absence of licensing cost (a major factor for the industry).
- Wide range of ready-made pre- and post-processing utilities.

FireFOAM is a LES (see Section 2.2 for a brief description of LES) based fire dynamics solver that uses Favre-filtered compressible Navier-Stokes equations [36] (see Section 2.3) and provides additional models for the treatment of turbulent

reactive flows [33], solid fuel pyrolysis [37], soot radiation [38] and transport of liquid water sprays and surface wetting [39].

Next, the governing equations are presented, followed by a brief discussion of the LES technique. Then, the filtered equations, relevant to FireFOAM (and LES), are discussed. Finally, turbulence modelling is addressed.

2.1 Governing equations

The instantaneous continuity, momentum and energy equations for a compressible fluid can be written, in indicial notation, as:

$$\frac{\partial \rho}{\partial t} + \frac{\partial \left(\rho u_j\right)}{\partial x_j} = 0 \tag{2.1}$$

$$\frac{\partial \left(\rho u_i\right)}{\partial t} + \frac{\partial \left(\rho u_i u_j\right)}{\partial x_j} = -\frac{\partial \left(p\right)}{\partial x_j} + \frac{\partial \tau_{ij}}{\partial x_j} + \rho g_i \tag{2.2}$$

$$\frac{\partial \left(\rho e_0\right)}{\partial t} + \frac{\partial \left(\rho u_j e_0\right)}{\partial x_j} = -\frac{\partial \left(u_j p\right)}{\partial x_j} - \frac{\partial q_j}{\partial x_j} + \frac{\partial \left(u_i \tau_{ij}\right)}{\partial x_j} \tag{2.3}$$

where, ρ is the mass density, u_i is the ith component of velocity, p is the pressure, g_i is the ith component of the gravity vector, τ_{ij} is the viscous stress tensor which for a Newtonian fluid, assuming Stokes Law for mono-atomic gases, is given by:

$$\tau_{ij} = 2\mu \left(S_{ij} - \frac{1}{3} S_{kk} \delta_{ij} \right) \tag{2.4}$$

where, μ is the dynamic viscosity and the rate of strain tensor S_{ij} is defined by:

$$S_{ij} \equiv \frac{1}{2} \left(\frac{\partial u_i}{\partial x_j} + \frac{\partial u_j}{\partial x_i} \right) \tag{2.5}$$

e_0 is the total energy and is defined by:

$$e_0 \equiv e + \frac{u_k u_k}{2} \tag{2.6}$$

here, e is the specific internal energy. The heat-flux, q_j, is given by Fourier's law:

$$q_j = -\lambda \frac{\partial T}{\partial x_j} \tag{2.7}$$

here, T is the temperature and λ is the thermal conductivity.

2.2 Large Eddy Simulation (LES)

There are three major techniques for numerically analyzing fluid dynamics: DNS [40], LES [41] and RANS [42] Simulations.

Overall, DNS (RANS) is the most (least) accurate but is also the most (least) expensive. In DNS, the governing equations (Section 2.1) are solved without any change and all the scales of a turbulent flow (from integral to Kolmogorov) are resolved on the grid whereas in RANS time averaged equations are employed and none of the scales are represented on the grid. The time averaging operation leads to extra terms in the equations, that represent the effects of turbulence on the averaged flow. Models (called turbulence models) are required to represent the extra terms and over the past decades a wide range of them have been developed [42] but to date no universal model has appeared; some work for one type of flow and some for a different type. The reason for such a problem stems from the fact that turbulent scales (especially the larger scales that have the most turbulent kinetic energy) depend heavily on the system/device under investigation. Due to this turbulence modelling problem, RANS technique has been very unreliable and has lead to the

development of LES, which lies in between DNS and RANS both in terms of fidelity and computational expense.

In LES, not all the scales of a turbulent flow are resolved (like DNS), only the large energy-containing scales are resolved on the grid (which as already mentioned depend heavily on the system/device being investigated) and the effects of the smaller scales (called sub-grid scales) on the resolved scales are represented by a SGS turbulence model. Unlike the larger scales the smaller scales are expected to be more universal, and hence make LES a superior numerical tool when compared to RANS.

In the present study, DNS was used in a preliminary series of highly-resolved simulations of RTI (see Chapter 3) and for predicting thermal instability onset in a reduced version of Configuration 2 without the transition and turbulent regimes. LES was then used in subsequent simulations of Configuration 2 and Configuration 3 (see Chapters 4 and 5).

2.3 Filtered governing equations

Favre-filtered mass, momentum and energy equations [36], solved by FireFOAM (for the non-reacting cases used in this study), are written below.

Mass:

$$\frac{\partial \overline{\rho}}{\partial t} + \frac{\partial (\overline{\rho}\widetilde{u}_j)}{\partial x_j} = 0 \tag{2.8}$$

Momentum:

$$\frac{\partial (\overline{\rho}\widetilde{u}_i)}{\partial t} + \frac{\partial (\overline{\rho}\widetilde{u}_i\widetilde{u}_j)}{\partial x_j} = -\frac{\partial \overline{p}}{\partial x_i} + \frac{\partial}{\partial x_j}\left(\overline{\rho}(\nu + \nu_{SGS})\left(\frac{\partial \widetilde{u}_i}{\partial x_j} + \frac{\partial \widetilde{u}_j}{\partial x_i} - \frac{2}{3}\frac{\partial \widetilde{u}_k}{\partial x_k}\delta_{ij}\right)\right) + \overline{\rho}g_i \tag{2.9}$$

Sensible Enthalpy:

$$\frac{\partial\left(\overline{\rho}\widetilde{h}_s\right)}{\partial t}+\frac{\partial(\overline{\rho}\widetilde{u}_j\widetilde{h}_s)}{\partial x_j}=\frac{\mathrm{D}\overline{p}}{\mathrm{D}t}+\frac{\partial}{\partial x_j}\left(\overline{\rho}\left(\alpha+\frac{\nu_{SGS}}{\mathrm{Pr}_{SGS}}\right)\frac{\partial\widetilde{h}_s}{\partial x_j}\right)-\frac{\partial\overline{q}_j}{\partial x_j} \tag{2.10}$$

State Relation:

$$\overline{P}=\overline{\rho}R\widetilde{T} \tag{2.11}$$

where $\widetilde{}$ is the Favre filter operator, ν is the kinematic molecular viscosity, ν_{SGS} is the SGS viscosity, Pr_{SGS} is the SGS Prandtl number, h_s is the sensible enthalpy and α the thermal diffusivity.

A combination of the PISO and SIMPLE (referred to as PIMPLE) solution algorithms were used for handling pressure velocity coupling. Additional information about the iteration procedure and discretization schemes can be found in [43].

2.4 Sub-Grid Scale (SGS) turbulence modelling

No explicit SGS model (e.g., Smagorinsky, Deardorff, WALE) was employed in this study, which essentially means that ν_{SGS} was set to zero. So, this technique can be described as Implicit Large Eddy Simulation (ILES) [44], wherein the dissipation at the higher wavenumbers was provided by the numerical scheme (or following Shur et al. [45] it can be called a coarse-grid DNS).

For a justification of SGS turbulence modelling strategy used here and a discussion on inverse energy cascade, two-way energy transfer, dynamic SGS models and the recent Non-linear Large Eddy Simulation (nLES) method, see Section 3.2 where the flow dynamics seen in RTI is used as a reference to highlight a major issue in designing appropriate SGS models for buoyancy dominated flows .

3: Rayleigh-Taylor Instability (Configuration 1)

Rayleigh-Taylor instability (RTI) is an interfacial instability that occurs when a high-density fluid is accelerated or supported against gravity by a low-density fluid [46, 47]. It is the latter situation, involving gravitational acceleration, that is germane to the present study.

Theoretically, it is possible to support a heavier fluid over a lighter fluid in the presence of gravity by maintaining a perfectly flat interface between the two fluids. However, in practice it is very difficult, if not impossible, to avoid small perturbations, which lead to an eventual displacement of the lighter fluid by the one that is heavier.

This instability is of fundamental importance in a wide range of applications, from fluidized beds, oceans, and atmosphere, to magnetic or inertial confinement fusion [48–50], and to astrophysics [51] e.g., Type Ia Supernovae [52]. Consequently, it has been subjected to intense research over the past several decades [53–55].

Unfortunately, several questions, even the most basic ones, regarding this instability are far from settled [51, 56]. So, before moving any further it should be noted, that the aim here is not to address, or even discuss, any of the RTI related questions; but to use it as a tool to first thoroughly verify the solver and then

to learn about the various stages involved in the growth of RTI. It will also help in guiding e.g., the grid design for eventual relatively larger calculations. So, this chapter starts off with discussions related to early-time dynamics, which includes a brief presentation of LST [57] and results from two dimensional single mode DNS of RTI, wherein the major objective was code verification. Subsequently, late-time dynamics is discussed.

3.1 Early-time dynamics

3.1.1 Linear Stability Theory (LST)

If the initial interfacial perturbations are small, so that the higher order terms (HOT) can be neglected in a Taylor series expansion, then the early flow stages can be described by the linearized form of the governing equations [57]. The result is that the perturbations grow exponentially with time as follows [56]:

$$H(t) = a_0 \cosh(nt) - \frac{u_0}{n} \sinh(nt) \tag{3.1}$$

where, a_0 is the initial amplitude of the perturbation, u_0 is the initial velocity at the interface and t is the time.

The exponential growth factor for two incompressible, immiscible, inviscid fluids without any surface tension, with an inifinite density gradient at the interface; can be written as [57] (it will be called LST from here on):

$$n = \sqrt{\mathrm{A}gk} \tag{3.2}$$

where, k is the wavenumber of the initial perturbation, g is gravitational acceleration and A is the Atwood number, defined as $(\rho_1 - \rho_2)/(\rho_1 + \rho_2)$; ρ_1 and ρ_2 are the densities

of the heavier and lighter fluids, respectively. Which implies that as the wavenumber increases the growth factor also increases. But if the fluids are viscous then the smaller scales (or higher wavenumbers) are not allowed to grow as fast and that leads to the concept of a most-dangerous-mode, which basically is a mode/wavenumber that corresponds to maximum amplification. The growth factor in that case is given as [58] (and will be called LSTV):

$$n = \sqrt{Agk + \nu^2 k^4} - \nu k^2 \tag{3.3}$$

The most-dangerous-mode, k_{md}, can then be extracted as follows [58]:

$$k_{md} = \frac{1}{2}\left(\frac{\mathrm{A}g}{\nu^2}\right)^{\frac{1}{3}} \tag{3.4}$$

If mass diffusion is incorporated then the expression for growth factor becomes [58] (will be called LSTVMD):

$$n = \sqrt{\frac{Agk}{\psi} + \nu^2 k^4} - (\nu + D)k^2 \tag{3.5}$$

where, D is the molecular mass diffusivity and ψ is a function of A and b is equal to $1/k\epsilon$, with $\epsilon = 2(Dt)^{1/2}$. Variation of ψ as a function of b^{-1} for various values of A is presented in Figure 3.1, see [58] for details. Clearly with mass diffusion the growth factor changes with time.

Just like viscosity, inclusion of mass diffusion paves way for another special wavenumber called the cut-off wavenumber, k_{co}, above which a perturbation is not allowed to grow. In the present study $D = 0$, however, thermal diffusivity (α) is not and α is expected to have the same effect as D [59]. So, Equation (3.5) can be re-written for the purpose of this investigation as (this model will be called LSTVTD):

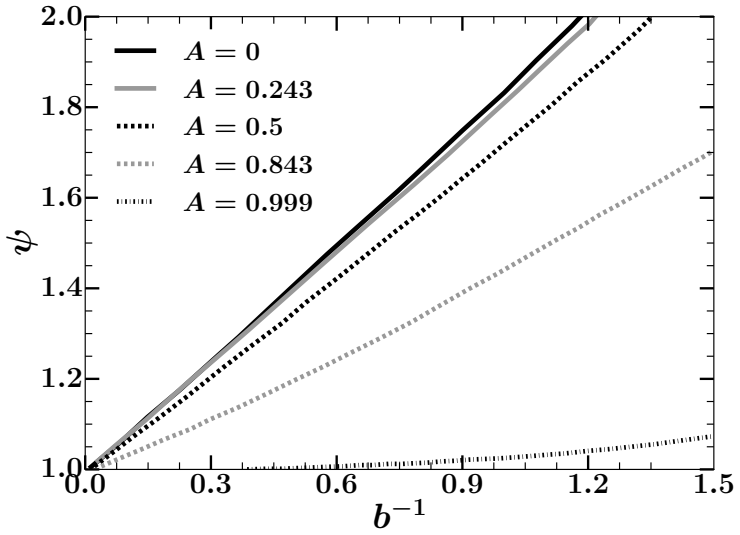

Figure 3.1: Variation of ψ as a function of b^{-1} for different values of A.

$$n = \sqrt{\frac{Agk}{\psi} + \nu^2 k^4} - (\nu + \alpha)k^2 \tag{3.6}$$

Equations (3.2), (3.3) and (3.5) are plotted in Figure 3.2 for a system with air at temperatures of 300 and 400 [K]. Note that ψ was set equal to 1, which relates to very early stages when the interface thickness, due to thermal diffusion, is small. It is clear that inclusion of α plays a major role and brings down the most-dangerous-mode, roughly, by a factor of two. Note that with time thermal diffusion shows its effects even more [58] since n is connected to t through ψ, b and ϵ.

3.1.2 Two dimensional single mode Direct Numerical Simulations (DNS)

Even though FireFOAM has already been verified and validated for a range of buoyancy dominated problems [33, 37–39], it has not been specifically used to

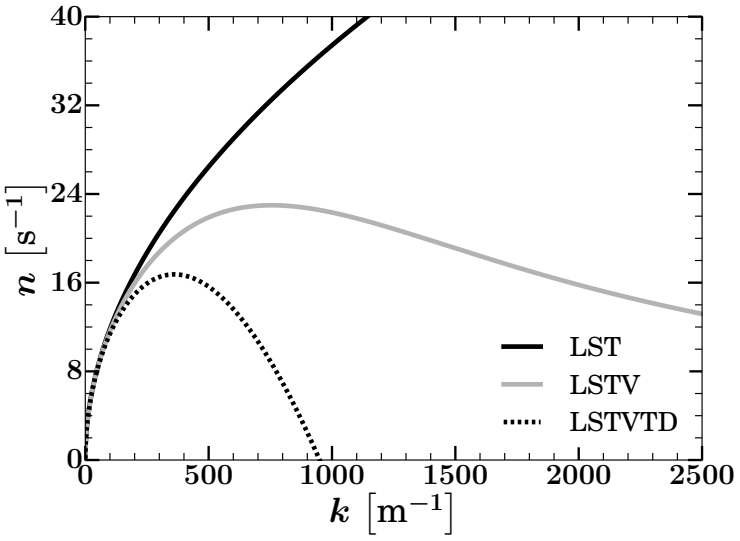

Figure 3.2: Growth factor as a function of wavenumber (k); predicted by LST, LSTV and LSTVTD.

investigate instabilities in any of the prior studies. Hence it was thoroughly verified against LST, both in terms of getting the exponential perturbation growth as well as identifying the most dangerous mode.

Furthermore, during the course of these simulations the minimum grid resolution required to capture these instabilities, which will play an important part in the relatively more expensive three dimensional calculations presented in Chapters 4 and 5, will also become clear.

3.1.2.1 Numerical setup

The width of the domain used was 2λ and the height was 4λ. Which means that when the wavelength or wavenumber was changed/scaled, e.g., in order to identify the most dangerous mode, the domain also scaled up or down with it, which was necessary to keep the computational expense manageable, especially for simulations

involving relatively higher wavenumbers.

Similarly, the initial perturbation height was taken to be 0.04λ (following [60]), in other words it was four percent of lambda. Note that the definition of perturbation height is the sum of bubble height (H_B) and spike height (H_S), where H_B (H_S) is defined as the height of perturbation above (below) the initial mean interface location, see Figure 3.3 for visualization. Physically, H_B (H_S) is connected to penetration of the lighter (heavier) fluid into the heavier (lighter) fluid.

The initial interface thickness was two percent of λ. For the variation of quantities (temperature in this study) across the interface thickness, an error function profile was used in e.g., [51,56,60,61], an exponential variation was utilized in [62,63] and a cosine function was employed in [64]. In this study a hyperbolic tangent function was used and was found to be sufficient for initializing the diffusion layer:

$$T = T_2 - (T_2 - T_1)(1 + \tanh(\frac{2\pi}{\delta}(y + a_0 \cos\left(\frac{2\pi x}{\lambda}\right))))/2 \tag{3.7}$$

Where, T_2 (T_1) is the temperature of the lighter (heavier) fluid. δ is the initial interface thickness, a_0 is the initial amplitude of the perturbation and λ is the wavelength of the initial perturbation.

Following [56,61], periodic boundary conditions were employed in the horizontal i.e., y direction; and slip walls were used for the top and bottom boundaries in the z (vertical) direction, .

Cell size used in the horizontal direction (Δy) was 0.004λ and in the vertical direction (Δz) was 0.002λ i.e., $\Delta z = 0.5\Delta y$, resulting in 250 grid points across one perturbation wavelength and 20 (10) grid points across the initial perturbation

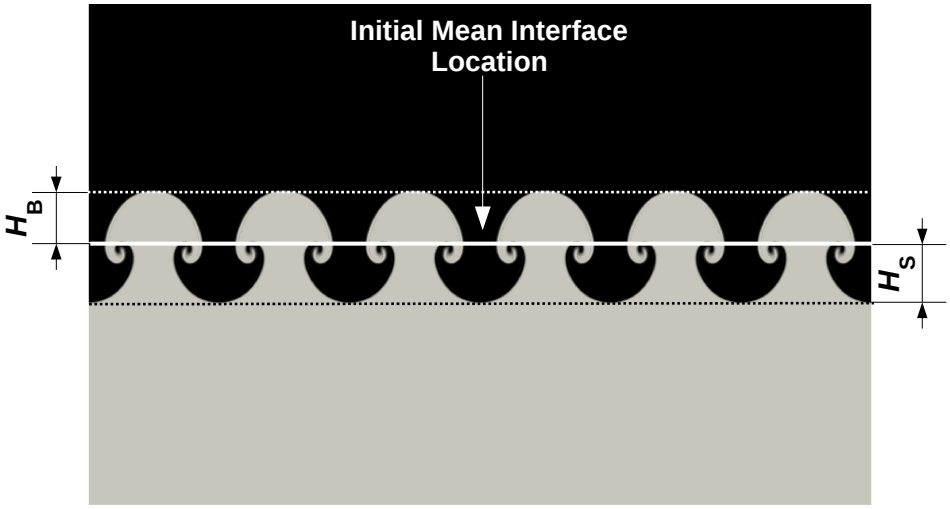

Figure 3.3: Definition of bubble height (H_{B}) and spike height (H_{S}), where heavy fluid is in black and lighter fluid is in grey.

amplitude (interface thickness). The initial interface thickness was resolved by five to eight grid points in prior studies [51, 56, 60, 61].

Keeping in mind, that LST is only applicable in the initial stages of flow development i.e., as long as the perturbation amplitude is roughly within 15 percent of λ; having a uniform grid density in the vertical direction, which spans 4λ, was considered unnecessary. So, in the vertical direction the cell size was kept constant and equal to 0.002λ for 0.4λ on both sides of the initial mean interface location (see Figure 3.3). Beyond that region the grid was stretched upto the walls, leading to a Δz of 0.04λ at the top and bottom walls.

In the coming sections it will be shown that the results using this grid were practically similar to those given by a grid having uniform cell size in the vertical direction.

3.1.2.2 Perturbation growth

As already described, in the initial stages of RTI the growth of a perturbation is exponential and can be described by LST. In order to verify FireFOAM a simulation was ran for $\lambda = 80$ [m] or $k = 0.0785$ and the peak to valley height (i.e., $H_{\mathrm{B}} + H_{\mathrm{S}}$) of the $(T_1 + T_2)/2$ or $(\rho_1 + \rho_2)/2$ isoline was monitored during the course of the simulation. In order do that all the cells having a temperature greater than and less than $(T_1 + T_2)/2$ were marked after every time step; and H_B (H_S) was set to be equal to the maximum (minimum) z value in the former (later) collection of cells. Despite the fact that the perturbation growth (or the peak to valley height of the $(T_1 + T_2)/2$ isoline) provided by this algorithm varied on a cell by cell basis and was not continuous, the results compared very well with LST (discussed below).

A comparison of the perturbation growth from the DNS using FireFOAM (at every twentieth time step) with that given by LST can be seen in Figure 3.4. The initial agreement is very good and then there is a discrepancy which is simply because when the perturbation amplitude becomes comparable to the wavelength (e.g when $(H_{\mathrm{B}} + H_{\mathrm{S}})/\lambda > 0.1$), non-linear effects become important (similar results are reported in [56, 60, 62]). Temperature contours at $t = 0$ and $t = 5$ [s] (at $t = 5$ [s] the numerical solution starts to show sufficient deviation from the growth given by LST) are shown in Figure 3.5.

Note that the reason for choosing a low wavenumber was that at such low values viscous and thermal diffusion effects become negligible (see Figure 3.2) and n can simply be represented as in Equation (3.2), which can in turn be plugged into

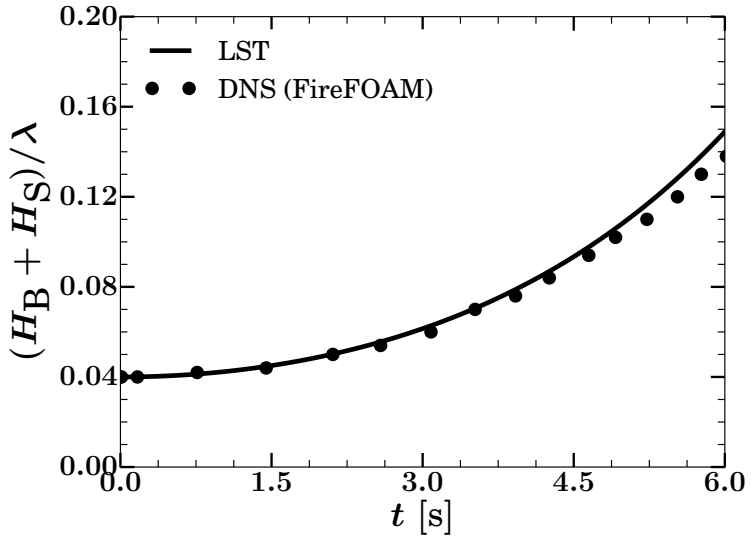

Figure 3.4: Comparison of the growth/amplification of a perturbation, with time, given by DNS; with that given by LST.

Figure 3.5: Temperature contours, at $t = 0$ [s] (left) and at $t = 5$ [s] (right), for the RTI simulation with $\lambda = 80$ [m] (or $k = 0.0785$ [m^{-1}]). Heavy (light) fluid is in black (gray). Black (gray) corresponds to $T = 300$ (400) [K].

Equation (3.1) to get the analytical growth of a perturbation. Similar strategy to avoid any kind of diffusion effects was used in [56], where the chosen wavenumber was $7.67e^{-04}$.

The sensitivity of the solution presented in Figure 3.4, to grid size as well as

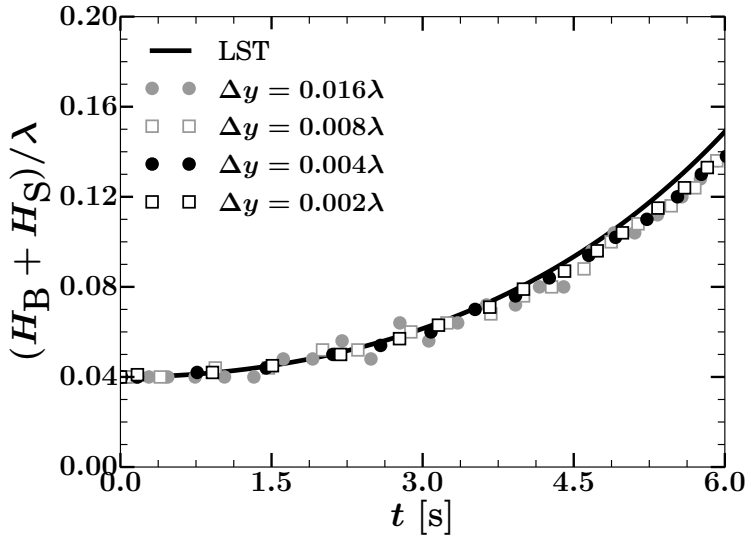

Figure 3.6: Growth/amplification of a perturbation, with time, given by LST and by DNS with four different grid resolutions.

cell size distribution was investigated. The perturbation growth for four different grid sizes can be seen in Figure 3.6. A reduction of Δy below 0.004λ did not have any tangible effect on the results.

Similarly, comparison between the solution produced using a uniform grid with that given by a grid that was stretched in the vertical direction is presented in Figure 3.7. The grid with $\Delta y = 0.008\lambda$ was employed for this exercise, which is the reason for some discrepancy with LST in Figure 3.7. No differences can be observed indicating that grid stretching did not have any effect on the results. Note that the ratio of the stretched grid cell count to the uniform grid cell count was roughly 0.3, which lead to considerable savings in computational cost.

Apart from the sensitivity of the solution to the grid, effects of domain size were also investigated in order to make sure that the boundaries were not affecting

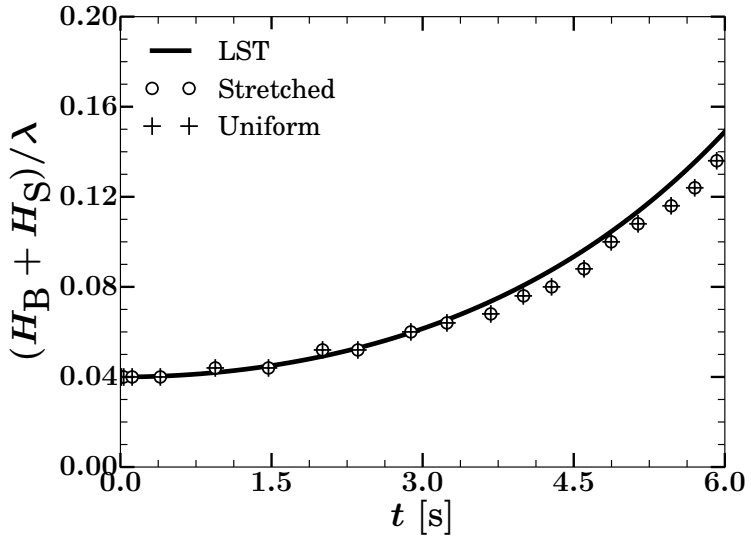

Figure 3.7: Growth/amplification of a perturbation, with time, given by LST and by DNS with a uniform grid and a grid that was stretched in the vertical direction.

the overall solution. Again the grid with $\Delta y = 0.008\lambda$ was used to keep the computational cost down. Results are presented in Figure 3.8. The domain size $2\lambda \times 4\lambda$ was found to be sufficient to avoid any interaction with the boundaries.

3.1.2.3 Most Dangerous Mode

Another way of testing a solver is by constructing the growth factor curve either only with viscosity or with both viscosity and thermal diffusion. Growth factors extracted from ten different initial perturbations without any thermal diffusion are plotted in Figure 3.9 along with the classic LST and LSTV. FireFOAM was able to reproduce the growth rate curve with a reasonable accuracy.

Similarly, the growth rate curve, when thermal diffusion effects were considered along with viscosity, extracted from FireFOAM is compared with LSTVTD in Figure 3.10. As already described, when mass/thermal diffusion effects are incorpo-

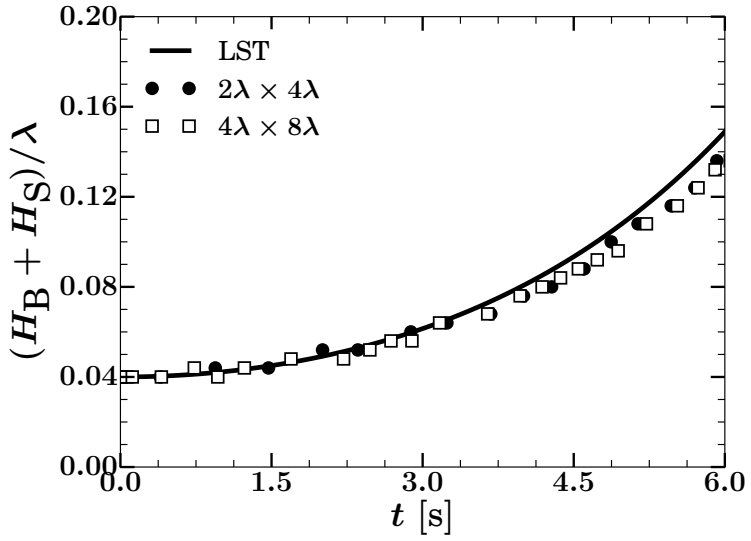

Figure 3.8: Growth/amplification of a perturbation, with time, given by LST and by DNS with two different domain sizes.

rated into LST ([58]), n for every wavenumber starts to vary/decrease with time through ψ. In addition, LST is only valid for relatively small perturbation heights. Furthermore, LSTVTD is only ten percent accurate. All these issues make it tricky to compare the numerical data points with Duff et al.'s expression i.e., LSTVTD. Note, however, that comparisons with LSTVTD have been made in the literature, see e.g., [56]. But keeping in mind that the solver has already been able to reproduce the exponential perturbation growth with time (Figure 3.4) and the growth factor curve not including the effects of thermal diffusion (Figure 3.9), it was decided (due to time constraints) to compare the the numerical data points with LSTVTD keeping $\psi = 1$. Clearly, there is a discrepancy in Figure 3.10 but the most dangerous mode still compares well.

Overall, the solver has compared very well with LST and LSTV quantita-

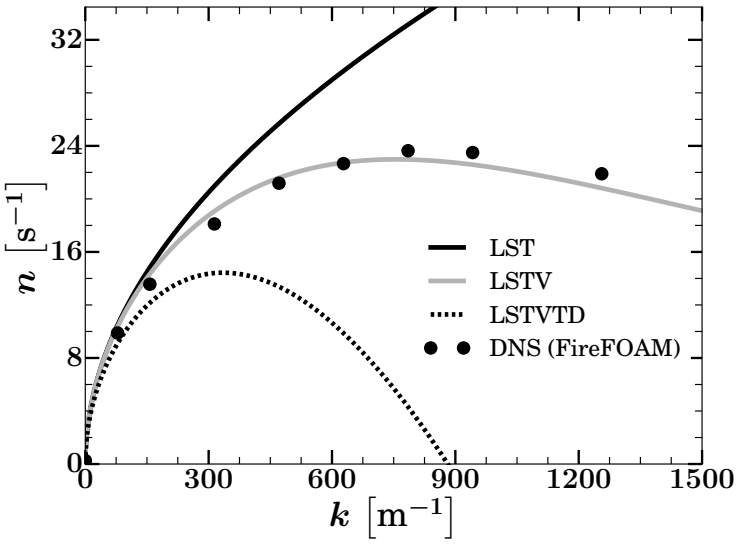

Figure 3.9: Comparison of the growth factor, as a function of wavenumber, given by DNS having zero thermal diffusion; with that given by LST, LSTV and LSTVTD.

tively and with LSTVTD qualitatively, and seems suitable for handling flow problems/physics of this kind.

3.2 Late-time dynamics

The tests so far were limited to the short-time behaviour of RTI. We now turn to a study of the long-time behaviour, as it resembles the kind of dynamics seen in the recent experiments e.g., with the stationary burners [1]. Briefly or crudely, in Figure 1.2 smaller streaks in the BL combine/couple to produce bigger and bigger structures.

Similarly, in RTI: at early times, the perturbations grow in a fairly independent fashion (which we have already seen in e.g., Figure 3.5). Then secondary Kelvin-Helmholtz Instability (KHI) appears in the shear layers between individual structures and the local quiescent fluid. After that the structures start interacting

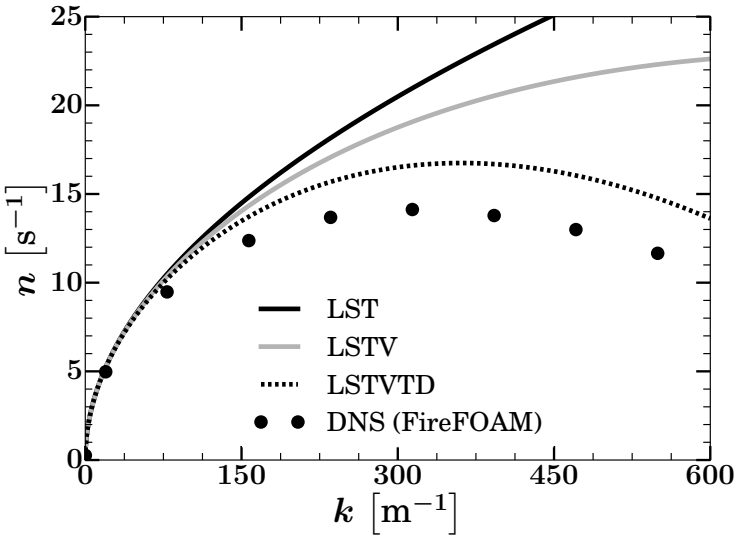

Figure 3.10: Comparison of the growth factor, as a function of wavenumber, given by DNS including the effects of thermal diffusion; with that given by LST, LSTV and LSTVTD.

with each other. At which point, the range of scales in the mixing layer increases rapidly, generating more mixed fluid within the layer, which is generally referred to as mixing transition, see Cook & Dimotakis [60]. Post transition, the large scales in the flow (bubble/spike diameters) continue to increase until the mixing region becomes fully turbulent [61].

A two-dimensional case was setup in FireFOAM to simulate some of these stages. Clearly, by definition turbulence is three dimensional and would not have been able to evolve correctly in a two dimensional configuration, but it should be noted first that this simulation is qualitative and second, a similar setup was used in [56].

The domain used was $8\lambda \times 16\lambda$, initial perturbation height (a_0) used was 16

percent of λ and the initial interface thickness (δ) was 8 percent of λ. Regarding the grid, the interface was resolved with twenty grid points, initial perturbation was resolved with fourty grid points, the horizontal wavelength with 125 points. Again, Δy (horizontal direction) was set to be equal to $2\Delta z$ (vertical direction). Overall, the grid had four million cells.

Most of the stages described above were recovered in this simulation and are presented in Figure 3.11 in the form of temperature contours. In Figure 3.11a we have the initialization, Figure 3.11b shows simulation time upto which the structures grow independently, KHI appears in Figure 3.11c (note that interaction between the structures is still not strong enough), interaction between the structures can be observed in the two subsequent contours (Figures 3.11d and 3.11e) and the final two contours (Figures 3.11f and 3.11g) seem to show a post transition state. Note the presence of roughly four structures in the gray fluid in the bottom contour, whereas the simulation started with eight of them. This appearance of bigger scales is consistent with the description above and is also similar to the flame dynamics seen e.g., with stationary burners, in Figure 1.2. Qualitatively, FireFOAM has been able to reproduce various stages in RTI.

Before moving on to Configuration 2 an important point regarding turbulence modelling can be made. RTI is a major challenge when it comes to designing SGS models. As already illustrated, in RTI flows, motion occurs first at the smallest dynamically significant scales, where perturbations at the density interface cause a misalignment of the pressure and density gradients, giving rise to baroclinic torque $\sigma = -(\nabla\rho \times \nabla p)/\rho^2$ that sets the system in motion. This movement creates sec-

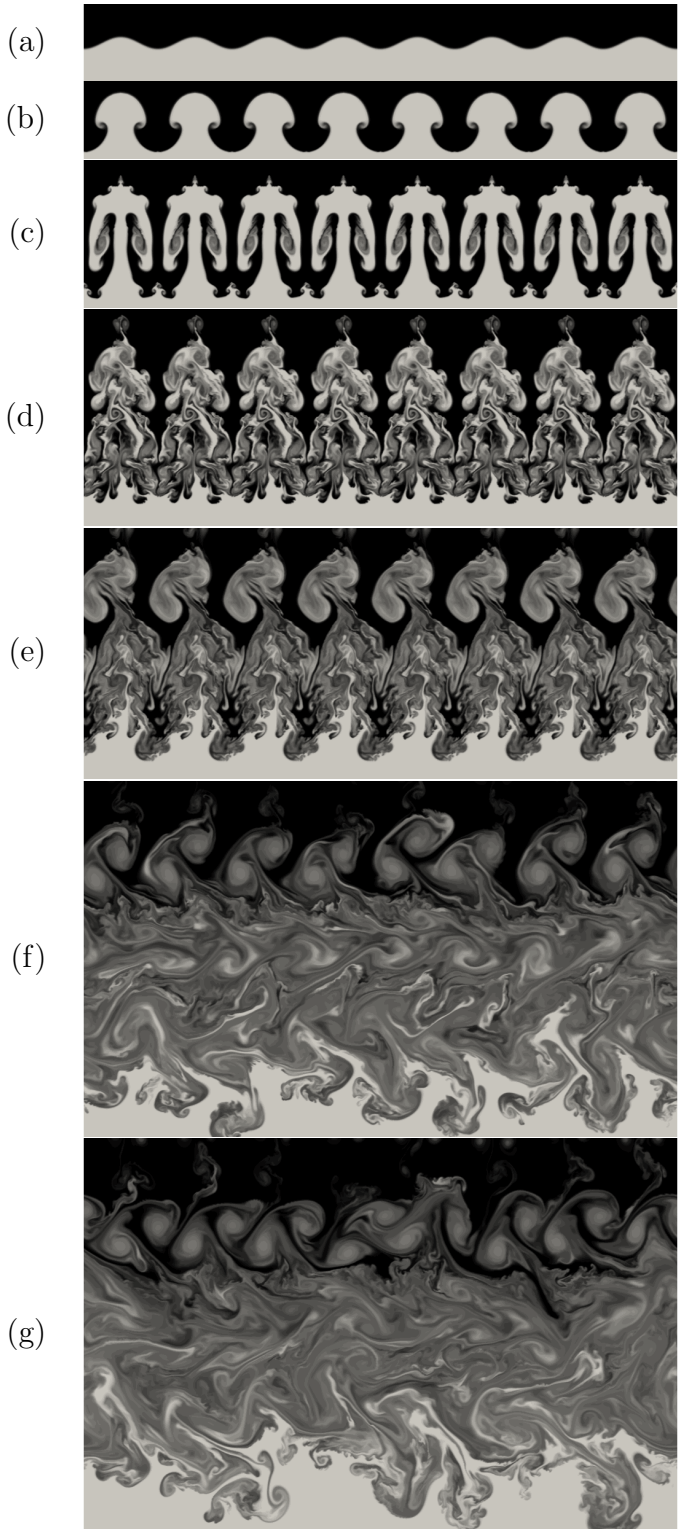

Figure 3.11: Various stages in the evolution of RTI. See text for details.

ondary KHI in the shear layers. Both the RTI and KHI transfer kinetic and scalar energy from the small scales to successively larger scales in the system, through an inverse cascade process, i.e., in a direction opposed to the usual forward cascade of Kolmogorov's turbulence theory. As the bubbles and spikes grow, they begin to combine in a nonlinear fashion due to the coupling between the buoyancy and inertial forces. At a later time, mixing transition is followed by a fully turbulent flow. Consequently, mixing layer dynamics become dominated by vortex stretching and a forward cascade of kinetic and scalar energies, which drives the creation of smaller scales [65, 66]. Overall, we have a two-way exchange of energy.

And just like RTI, buoyancy dominated flows (subject of this study) also involve a two-way energy exchange, which is not correctly captured by most of the LES models, see Blanquart and Pitsch [67] and Burton [65, 66] for a discussion. Apparently, Burton's nLES is the only method (which has appeared fairly recently) that is expected to handle problems of this kind accurately.

So, we plan to incorporate Burton's nLES in the future. But for the purpose of this study, as already mentioned in Section 2.4, ν_{SGS} was set equal to zero. We were relying on the numerical schemes to act as SGS models. This choice certainly needs to be re-visited but ideas of this nature have already been used to produce some quality results, see e.g., [61, 68, 69].

4: Low speed flow over a hot isothermal semi-infinite horizontal plate (Configuration 2)

In this chapter Configuration 2 is carefully analyzed in order to understand the flame structure/dynamics in wildfires and the relative weight of momentum-driven and buoyancy-driven motions.

A number of similarities were observed by Gilpin et al. [17] between this problem and that of the Gortler instability on a concave wall even though the source of the instability in the case of the latter is centrifugal force and in the case of the former (thermal instability) is the buoyancy force.

First, the general physical and numerical case setup for these horizontal plate simulations is presented and then the results from DNS, done for capturing the onset of the thermal instability are elucidated. After that various terms in the streamwise vorticity equation are analyzed in order to identify the important contributors to the generation/evolution of streamwise vorticity at the onset. The evolution of the structures from their onset to the turbulent free convection regime (through the transition regime) is then discussed, based on the results generated using LES. Finally, results from some more simulations are detailed to provide additional insight.

4.1 Physical and numerical setup: General features

The free-stream air flow for most cases had a temperature of 300 [K]. Plate temperature was varied for different cases but was mostly chosen such that there was a thermal instability inside the domain.

The computational domain, along with the boundary conditions, is shown in Figure 4.1. As can be seen, 0.1 [m] long empty free-stream region was used before the hot plate to avoid any interaction between the developing laminar BL and the inflow boundary. Periodic boundaries were used in the span-wise (y) direction, which essentially made the plate semi-infinite. The domain dimensions (L_x, L_y, L_z) will be specified, later, for each case separately, but L_x was always chosen such that Re_{L_x} was below the critical laminar-to-turbulent-flow-transition value of 5×10^5 so that there were no hydrodynamic instabilities inside the system.

4.2 Thermal instability onset

As already mentioned, predicting the onset of thermal instability in a Blasius BL has been a major problem both theoretically/analytically (starting with the work of Wu and Cheng [14]) and numerically, even with a tool like LES (used by Ojofeitimi [27]).

Some theoretical studies, e.g., the one by Moutsogluo et al. [16], provided results that were two to three orders of magnitude different from the experiments done by Gilpin et al. [17].

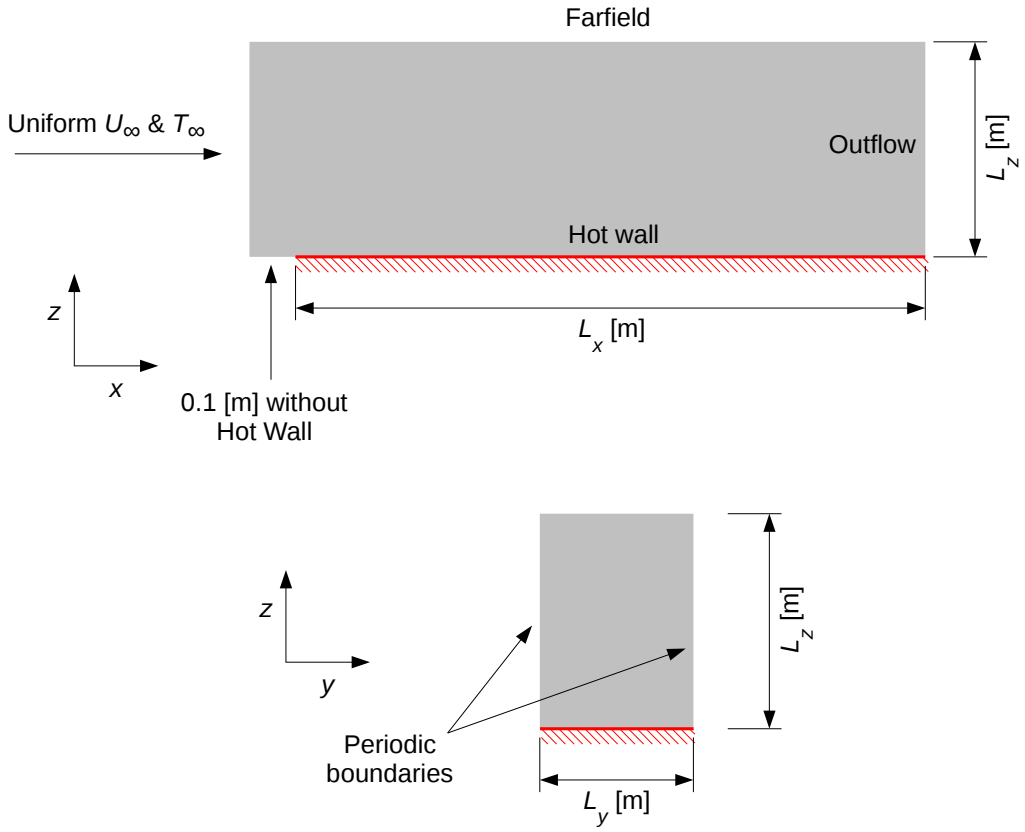

Figure 4.1: Flow over a hot flat isothermal plate, domain outline: side view (top) and back view (bottom).

Ojofeitimi [27] showed very good results, but there seems to be a discrepancy in that study. For the conditions used in [27] i.e., $U_\infty = 0.84$ [m/s], $T_\infty = 298$ [K] and $T_{plate} = 394.4$ [K] - the parameter $\mathrm{Gr}_x/\mathrm{Re}_x^{1.5}$ (identified e.g. in [17]) reaches a value of 100 (which is the critical value, for the onset of longitudinal vortices, identified by Gilpin et al. [17]) at $x = 0.25$ [m], but numerically the vortices appeared at $x = 0.5$ [m]. One simple reason for such a difference could have been the coarse grid that was employed by Ojofeitimi. The spacing in the x and y directions used in that study was 5 [mm]. And LSTVTD (i.e., Equation (3.6)) predicts, with $\psi = 1$, the most dangerous mode (wavelength) to be equal to 400 [m^{-1}] (15 [mm]) and the cut-off wavenumber (wavelength) to be 1000 [m^{-1}] (6 [mm]). So, there were only three grid points inside the most dangerous wavelength, which may not have been sufficient.

Considering all this a DNS was undertaken, in which L_x, L_y and L_z were set to values of 0.8, 0.1 and 0.1 [m], respectively. Regarding grid spacing: Δx and Δy were uniform and set to 2 and 1 [mm] respectively. In the wall normal direction (i.e., z) the grid was stretched from the wall with a Δz of 0.25 [mm] using a geometric ratio of 1.05. The resulting mesh had only 1.25 million cells.

Apparently, no thermal instability was seen at or close to $x = 0.25$, which was not consistent with the conditions formulated by Gilpin et al. [17] as they predicted the onset for the present conditions to be at $x = 0.25$ [m]. Specifically, the instability onset in this case was seen at $x = 0.75$ [m]. It is worth noting that the disagreement is worse than that obtained in Ojofeitimi's LES calculations.

In order to shed some light on this issue one more DNS was carried with plate

temperature of 550 [K] for which the $\mathrm{Gr}_x/\mathrm{Re}_x^{1.5}$ reached a value of 100 at $x = 0.15$ [m]. Numerically, the onset was seen at $x = 0.38$ [m]. The discrepancy was less severe but still very significant.

The reason for these discrepancies in the onset location was not clear. Artificial noise might be required to induce early transition consistent with the experimental data.

Nevertheless, it was decided to move on (this issue will be a part of future investigations), but before that the longitudinal structures visualized using an iso-surface of temperature with a value of 320 [K] are shown in Figure 4.2, for a visual evidence of the onset locations provided above. Note that the onset locations were also quantified by using the streamwise vorticity equation (see Section 4.3 for details).

It is worth mentioning that the wavelength (or wavenumber) of the instabilities seen in these simulations compared very well with the MDM predicted using LSTVTD for RTI. Such a comparison was not made by Ojofeitimi [27], probably due to an insufficient grid resolution.

4.3 The vorticity equation

The vorticity equation in Gibbs' notation can be written as:

$$\frac{\mathrm{D}\boldsymbol{\omega}}{\mathrm{D}t} = (\boldsymbol{\omega}\cdot\nabla)\,\mathbf{v} - \boldsymbol{\omega}\,(\nabla\cdot\mathbf{v}) + \frac{1}{\rho^2}\nabla\rho\times\nabla p + \nabla\times\left(\frac{\nabla\cdot\boldsymbol{\tau}}{\rho}\right) + \frac{1}{\rho}\nabla\rho\times\mathbf{g} \qquad (4.1)$$

where $\mathrm{D}/\mathrm{D}t$ is the total time derivative operator, $\mathbf{v}$ is the velocity field, ρ is the local fluid density, p is the local pressure, $\boldsymbol{\tau}$ is the viscous stress tensor and $\mathbf{g}$ represents the gravitational force.

Figure 4.2: Structures observed (top view) in the two DNS calculations. $T_{plate} = 394.4$ [K] (top) and $T_{plate} = 550$ [K] (bottom). $T = 320$ [K] isosurfaces.

The physical meaning of the various terms in Equation 4.1 is as follows:

1. The first term $(\boldsymbol{\omega} \cdot \nabla)\,\mathbf{v}$ on the right-hand side describes the stretching or tilting of vorticity due to the velocity gradients.

2. The second term $\boldsymbol{\omega}\,(\nabla \cdot \mathbf{v})$ describes stretching of vorticity due to flow compressibility (or expansion in this case)

3. The term $\nabla\rho \times \nabla p/\rho^2$ is the baroclinic term. It accounts for the changes in the vorticity due to the interactions of density and pressure variations.

4. $\nabla \times (\nabla \cdot \boldsymbol{\tau}/\rho)$, accounts for the diffusion of vorticity due to viscous effects.

5. The term $(1/\rho)\nabla\rho \times \mathbf{g}$ describes the effects of buoyancy.

Note that these tilting and stretching terms can only enhance the vorticity already present in the flow; they cannot generate new vorticity [70].

Since only the evolution of the streamwise vorticity is currently of interest,

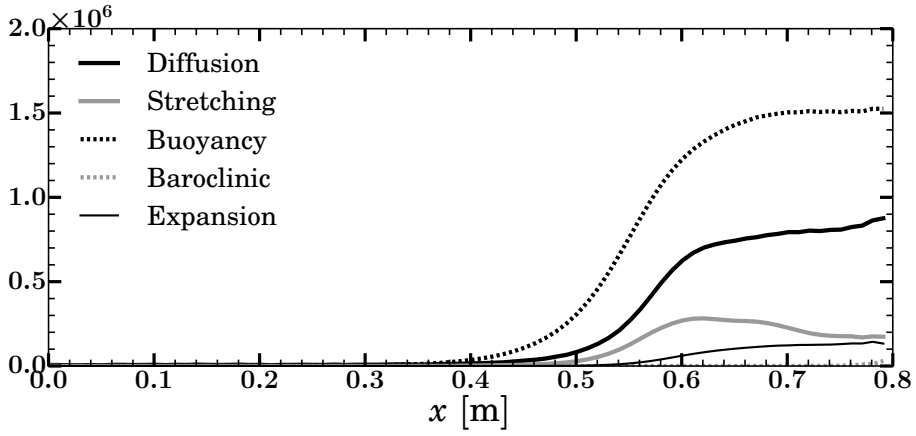

Figure 4.3: Flow over a hot isothermal plate at $T = 550$ [K]: Variation of different terms, in the streamwise vorticity equation, along the length of the plate.

attention was given only to the equation for ω_x, which is written below:

$$\begin{aligned}\frac{\mathrm{D}\omega_x}{\mathrm{D}t} = &\left(\boldsymbol{\omega}\cdot\nabla\right)v_x - \omega_x\left(\nabla\cdot\mathbf{v}\right) + \frac{1}{\rho^2}\left(\frac{\partial\rho}{\partial y}\frac{\partial p}{\partial z} - \frac{\partial p}{\partial y}\frac{\partial\rho}{\partial z}\right)\\ &+\left(\left(\frac{1}{\partial y}\frac{1}{\rho}\frac{\tau_{zx}}{\partial x} + \frac{1}{\partial y}\frac{1}{\rho}\frac{\tau_{zy}}{\partial y} + \frac{1}{\partial y}\frac{1}{\rho}\frac{\tau_{zz}}{\partial z}\right) - \left(\frac{1}{\partial z}\frac{1}{\rho}\frac{\tau_{yx}}{\partial x} + \frac{1}{\partial z}\frac{1}{\rho}\frac{\tau_{yy}}{\partial y} + \frac{1}{\partial z}\frac{1}{\rho}\frac{\tau_{yz}}{\partial z}\right)\right)\\ &+\left(\frac{1}{\rho}\left(\frac{\partial\rho}{\partial y}g_z - \frac{\partial\rho}{\partial z}g_y\right)\right)\end{aligned} \tag{4.2}$$

In order to investigate which of these terms dominate in the generation/evolution of streamwise vorticity, all of them were plotted (see Figure 4.3) along the length of the plate with $T = 550$ [K] (Figure 4.2). Even though the expansion term reduces vorticity it was plotted with an opposite sign here. Note that the three dimensional data was collapsed on a one dimensional line, simply by summing up the absolute values of each term in the $y - z$ planes along the length of the plate. Taking the absolute (or magnitude) of the values was necessary in order to avoid cancelling out vorticity due to the presence of CVP that are observed at early stages.

Clearly, Figure 4.3 shows that it is buoyancy that kick starts the generation

of thin horizontal structures close to $x = 0.4$ [m] and then all the other mechanisms follow e.g., once the vorticity enters the system due to buoyancy, it starts to diffuse due to viscosity and the reason why the diffusion term is larger than the others is because the flow is low speed and laminar like (we do have vortices but it is still almost laminar).

Due to heat transfer from the wall the flow continuously expands in this configuration i.e., $\nabla \cdot \mathbf{u}$ is always positive and hence the expansion term in the vorticity equation becomes finite as soon as vorticity enters the system (note that the expansion term as a whole will be negative but has been plotted with an opposite sign in the figure). Similarly, the interaction of multiple vortices leads to vortex stretching, here one can refer to the famous Taylor-Green vortex problem [71] to infer the dynamics. And finally the Baroclinic term is also expected to become finite soon, once the peaks of the vortices lift up enough.

4.4 Streamwise evolution of the structures

Doing a DNS covering all three regimes (laminar forced convection, transition and turbulent free convection) in this problem was not feasible so an LES was carried out.

In this case, free stream air flow had a velocity of 0.5 [m/s] and temperature of 300 [k]. The plate temperature used was 400 [K]. For these conditions the onset of thermal instability was expected to happen at $x = 0.15$ [m], according to Gilpin et al. [17].

L_x, L_y and L_z were set to values of 2, 0.3 and 0.6 [m], respectively. Grid

spacing used in the x and y directions was uniform and had a value of 5 [mm]. In the wall normal direction the grid was stretched from a value of 0.4 [mm] at the wall with a geometric progression having a ratio of 1.025. The mesh resolution was similar to that used by Ojofeitimi [27] and was not enough to resolve the MDM (and especially the cut-off wavenumber) sufficiently. At the same time, a DNS type high resolution mesh would have proved to be very expensive for this calculation as it includes all the regimes (laminar forced convection, transition regime and turbulent free convection).

The flow structures (visualized using an iso-surface of temperature with a value of 320 [K]) can be seen in Figure 4.4, and will be discussed in more detail later. The appearance of small structures and their subsequent combination/interaction/coupling leading to larger and larger structures can be clearly seen. The dynamics seems analogous to that seen in Figures 1.2 and 3.11.

For quantifying the dominant length scales in this setup a simple two dimensional fourier transform procedure was designed: basically separate one dimensional fourier transforms were generated for each horizontal cell layer in a $y-z$ plane. Before processing the data, the average temperature in each layer was subtracted from the corresponding temperature profiles, in order to get the fluctuation profiles; which were subsequently transformed to fourier space. The results from the application of such a procedure on three different $y-z$ planes located at $x = 1$, $x = 1.5$ and $x = 1.75$ [m]; can be seen in Figure 4.5. There is certainly no loss of information, at least spatially.

From Figure 4.5 it is clear that as we move along the length of the plate

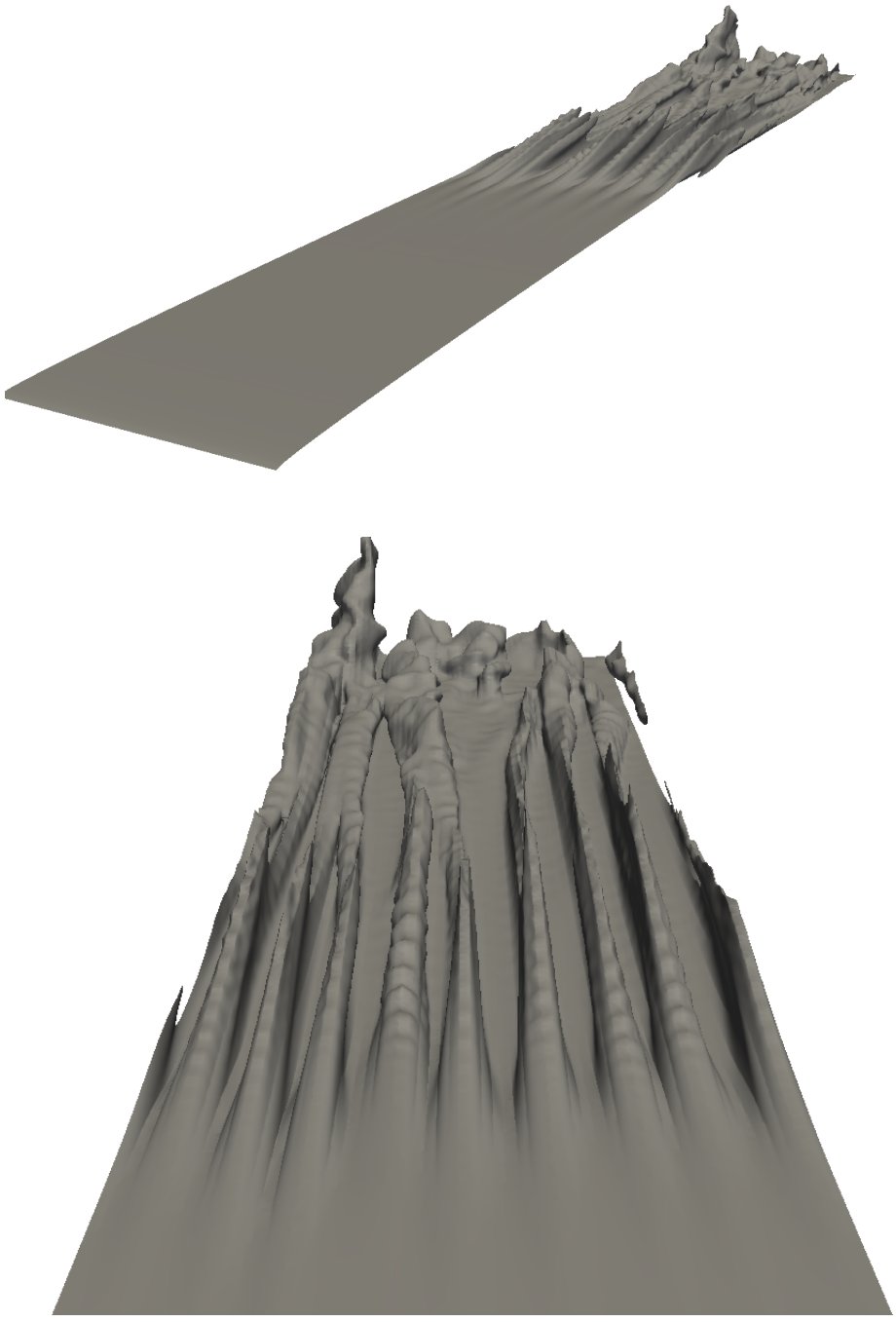

Figure 4.4: Flow over a hot flat isothermal plate: isosurface of T (320 [K]); perspective (top) and front view blow up of the instabilities (bottom).

the dominant mode/wavenumber decreases, indicating an inverse energy cascade (like the one seen in simulations related to RTI). Another observation, is that on plane 1, which is placed close to the appearance of the thin horizontal structures, the dominant mode/wavenumber is roughly 200 [m$^-$1]. For similar conditions (i.e., temperatures of 300 and 400 [K]) with viscosity and thermal diffusion LSTVTD roughly predicts the MDM to be 350 (see Figure 3.10). Overall, despite a coarse setup the agreement with LST is quite reasonable.

Evolution of different terms in the streamwise vorticity equation can be seen in Figure 4.6. Again it is clear that the instability results from the buoyancy term which sets everything else in motion.

We now turn to large scale features: large scales are expected to grow with the streamwise distance along the plate in this system and eventually reach a size comparable to the chosen span-wise domain size. See e.g., Cook, Cabot and Miller [61] and Cabot and Cook [51] for a discussion.

So, in order to investigate the larger scales (referred to as Flame Towers) observed in e.g experiments with stationary burners Figure 1.2, a more realistic configuration, with a hot strip instead of a plate, was utilized (discussed in the next Chapter).

4.5 Additional simulations

Some additional cases were simulated to provide more insight into this fundamental heat transfer problem. Results from a calculation with a plate temperature of 1500 [K] are shown in Figures 4.7 to 4.9. Horizontal (but not longitudinal) counter

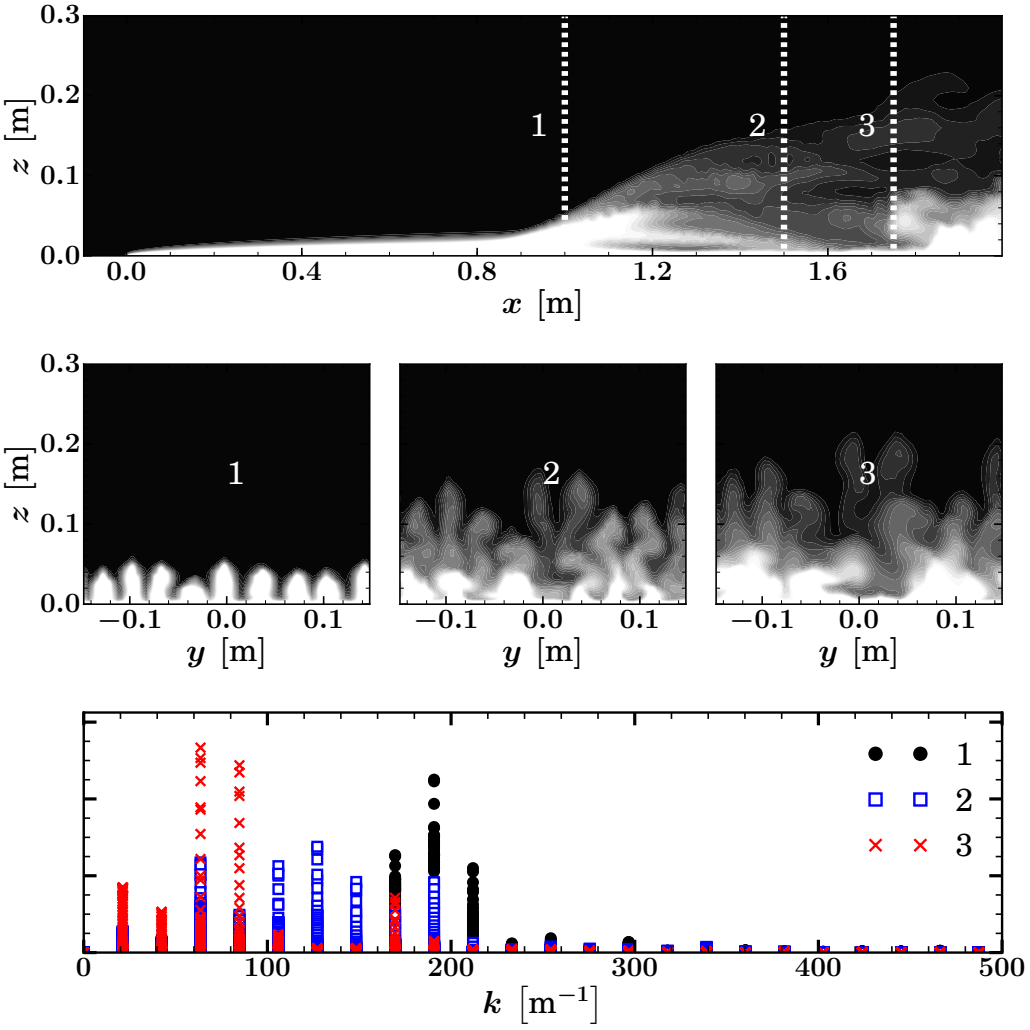

Figure 4.5: Flow over a hot isothermal plate at $T = 400$ [K]: Contours of temperature; at plane $y = 0$ [m] (top), at planes $x = 1$, $x = 1.5$ and $x = 1.75$ [m] (middle, from left to right) and two dimensional fourier transform of temperature at planes $x = 1$, $x = 1.5$ and $x = 1.75$ [m] (bottom). See text for details on the 2D FFT procedure. For the contours white (black) corresponds to $T > 320$ ($T = 300$) [K].

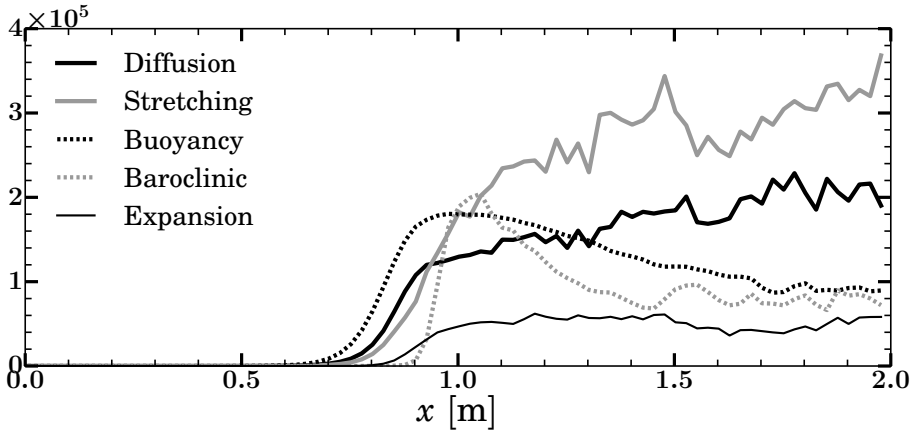

Figure 4.6: Flow over a hot isothermal plate at $T = 400$ [K]: Variation of different terms, in the streamwise vorticity equation, along the length of the plate.

clockwise structures can be seen due to the strength of the buoyancy force. Again the wavenumber (length scale) of the dominant structures keeps decreasing (increasing) with streamwise distance from the leading edge of the plate, but decreases (increases) relatively quickly (see Figure 4.7).

Plane 1 in Figures 4.5 and 4.8 has almost the same number of structures (roughly nine in the former and eight in the later) despite a five fold increase in the plate temperature. Which seems analogous to the insensitivity of the MDM to various parameters (due to the cube root), Equation 3.4, given by LSTV for RTI.

Another case was simulated wherein the gravity vector was rotated to be in the streamwise direction (but opposite to the flow direction) i.e $g = (-9.8, 0, 0)$ was used instead of $g = (0, 0, -9.8)$. It is clear from Equation (4.2) (and physically as well) that the buoyancy term plays no role in this case, since g_z and g_y both are zero here. And due to the absence of buoyancy, no structures were seen (see Figures 4.10 and 4.11) confirming buoyancy to be the single most important term in

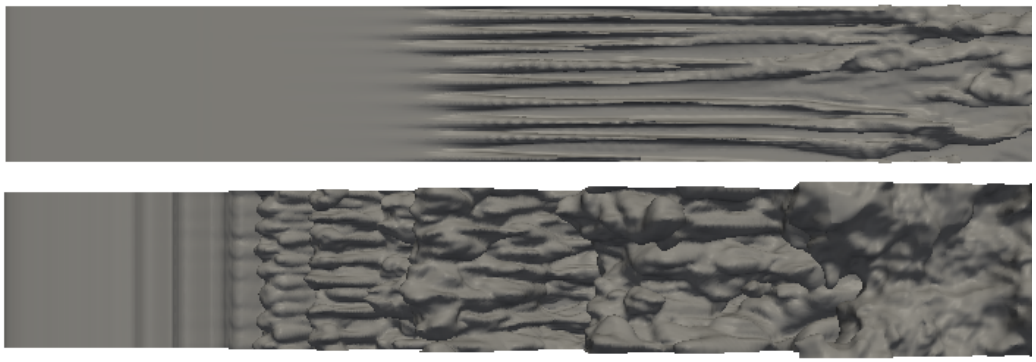

Figure 4.7: $T = 320$ [K] iso-surfaces: plate $T = 400$ [K] (top) and $T = 1500$ [K] (bottom).

the streamwise vorticity equation. Plots of various terms in the streamwise vorticity equation can be seen in Figure 4.12. As expected none of the mechanisms are active.

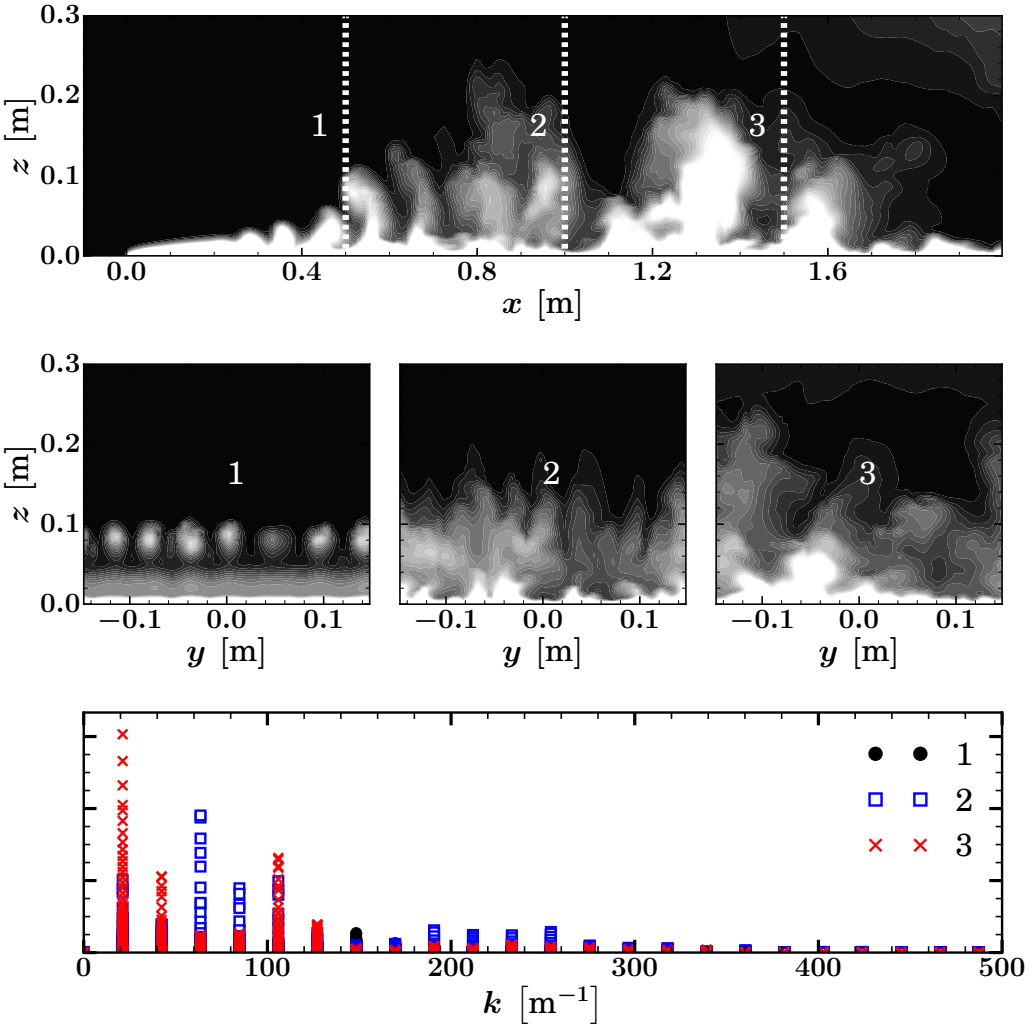

Figure 4.8: Flow over a hot isothermal plate at $T = 1500$ [K]: Contours of temperature; at plane $y = 0$ [m] (top), at planes $x = 0.5$, $x = 1.0$ and $x = 1.5$ [m] (middle, from left to right) and two dimensional fourier transform of temperature at planes $x = 0.5$, $x = 1.0$ and $x = 1.5$ [m] (bottom). For the contours white (black) corresponds to $T > 500$ ($T = 300$) [K].

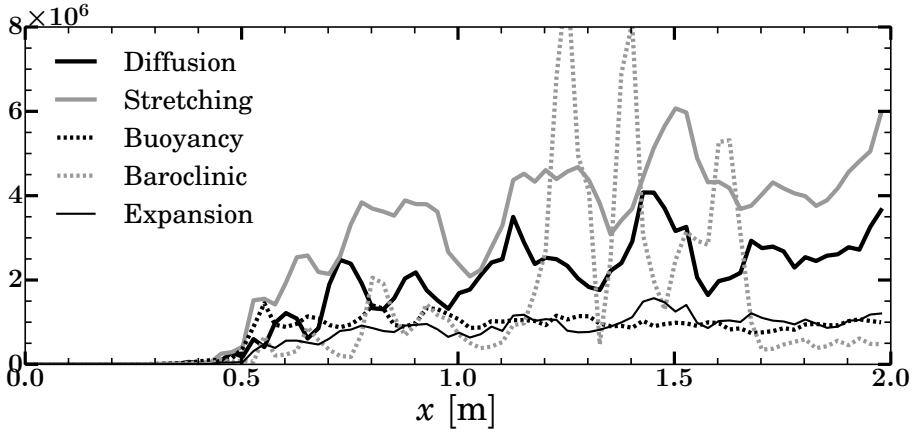

Figure 4.9: Flow over a hot isothermal plate at $T = 1500$ [K]: Variation of different terms, in the streamwise vorticity equation, along the length of the plate.

Figure 4.10: $T = 320$ [K] iso-surface: plate $T = 400$ [K] and $g = (-9.8, 0, 0)$ [m^2/s].

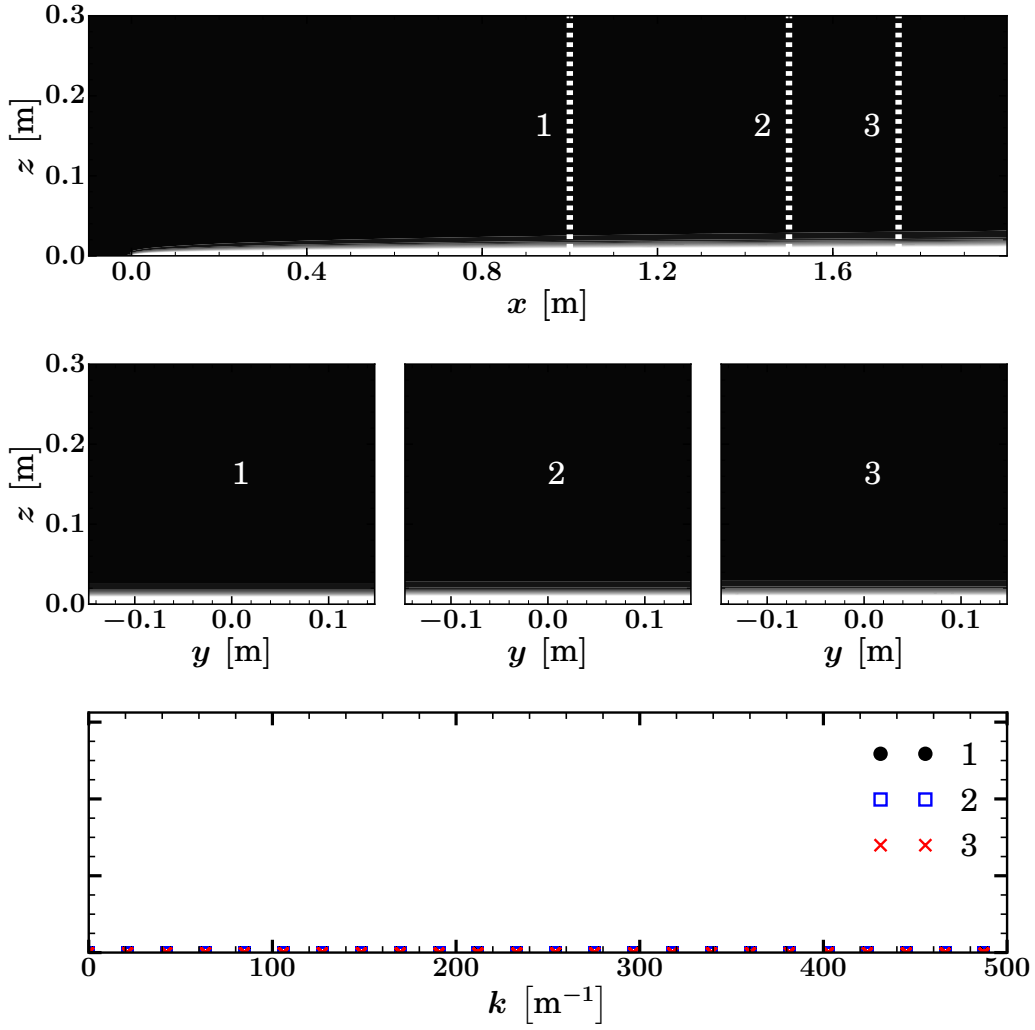

Figure 4.11: Flow over a hot isothermal plate at $T = 400$ [K] with gravity opposite to the freestream velocity: Contours of temperature; at plane $y = 0$ [m] (top), at planes $x = 1$, $x = 1.5$ and $x = 1.75$ [m] (middle, from left to right) and two dimensional fourier transform of T at planes $x = 1$, $x = 1.5$ and $x = 1.75$ [m] (bottom). For the contours white (black) corresponds to $T > 320$ ($T = 300$) [K].

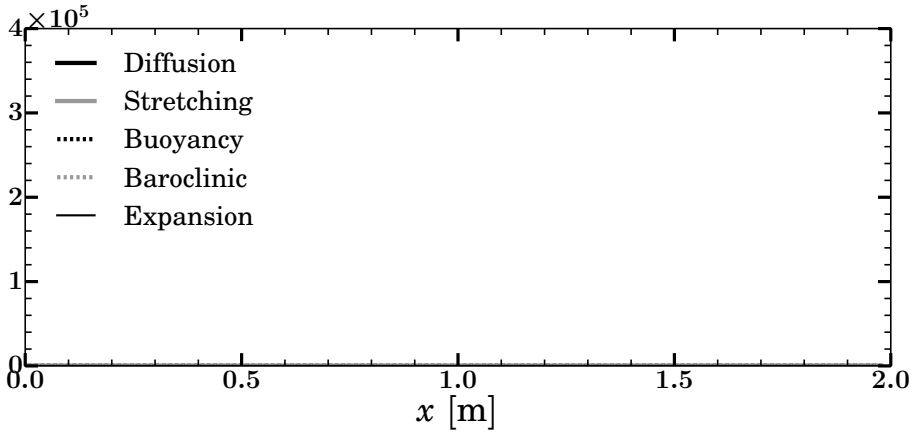

Figure 4.12: Flow over a hot isothermal plate at $T = 400$ [K] with gravity opposite to the freestream velocity: Variation of different terms, in the streamwise vorticity equation, along the length of the plate.

5: Low speed flow over a hot isothermal semi-infinite horizontal strip (Configuration 3)

To the best of our knowledge this configuration has never been studied either theoretically/analytically or using a quality numerical tool like LES. As already pointed out, there are a few related experimental studies, but there the heat source was a wire [28, 29]. Two dimensional numerical simulations have been carried out in two studies [30, 31] but e.g., the longitudinal structures were not allowed to develop by the two-dimensional model.

The physical and numerical setup is presented first, which is then followed by a brief discussion on a suitable thermal instability criteria. After that results from simulations carried out to understand the effects of incoming BL height and the streamwise length of the strip, are detailed.

5.1 Physical and Numerical setup

The free-stream air flow for all these cases had a velocity and temperature of 0.5 [m/s] and 300 [K], respectively. Strip temperature was kept constant and was equal to 1500 [K]

Outline of the computational domain, along with the boundary conditions,

is shown in Figure 5.1. Again, 0.1 [m] long empty free-stream region was used upstream of the solid plate to avoid any interaction between the developing laminar BL and the inflow boundary. Periodic boundaries were used in the span-wise (y) direction, which essentially made the strip semi-infinite, just like the plate. The domain dimensions $L_{upstream} + L_{strip} + L_{down}$ (total streamwise length), L_y and L_z used were 2, 0.6 and 0.3 [m], respectively. $L_{upstream}$ and L_{strip} were varied between cases and will be specified separately for each case.

Δx and Δy were kept uniform and had a value of 5 [mm]. In the wall normal direction the grid was stretched from a value of 0.4 [mm] at the wall with a geometric progression having a ratio of 1.025. Again the mesh resolution was similar to that used by Ojofeitimi [27].

5.2 Thermal instability onset criterion

Since, not much work has been done on this configuration there is no information on the onset criterion or even the critical parameter, analogous to $\mathrm{Gr}_x/\mathrm{Re}_x^{1.5}$ for the plate case.

Adaptation of the criterion for the case of a plate to the case of a strip gives $\mathrm{Gr}_{x_2}/\mathrm{Re}_{x_1}^{1.5}$ (see Figure 5.2 for information on x_1 and x_2) which seems to be ineffective. For instance, if $L_{upstream}$ was set to zero then the flat plate case is recovered with the plate length being equal to L_{strip}. Now, if $L_{upstream}$ was finite then before the strip starts Re_{x_1} would already have a finite value and it would take more effort from Gr_{x_2} to bring the stability parameter to the critical value (unknown for this configuration) for the onset of thermal instability. This is exactly opposite to what

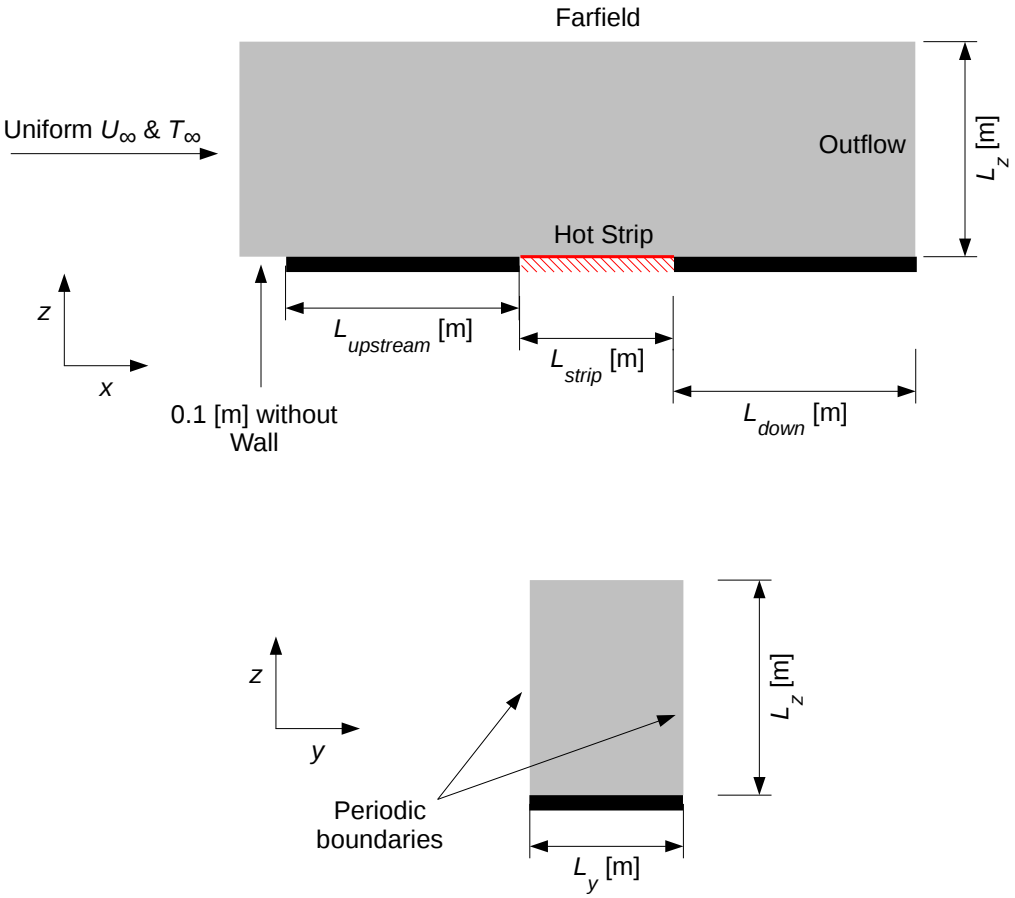

Figure 5.1: Flow over a hot flat isothermal strip, domain outline: side view (top) and back view (bottom).

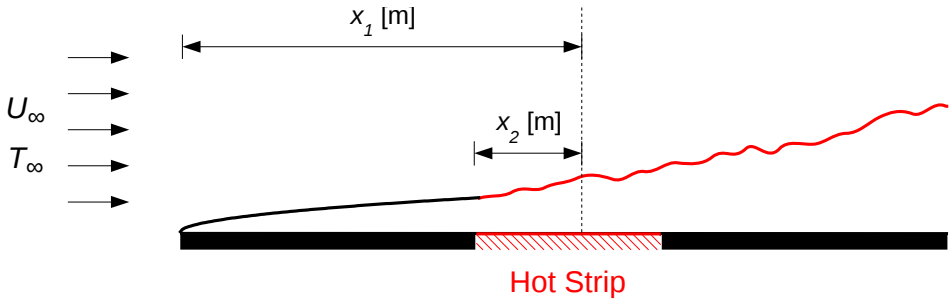

Figure 5.2: Outline for the case with low speed flow over a hot isothermal horizontal strip.

one would expect in a real situation since with a bigger incoming BL one expects to get the transition more easily and not the other way around, see Gorham [1].

So, in order to come up with a criterion, first a critical parameter would have to be determined for which one might resort to LST, just like Wu and Cheng [14] did for the flat plate case. Certainly, one necessary condition that such a parameter would have to satisfy is to reduce to the plate parameter if $L_{upstream} = 0$.

Once the parameter is determined, then a range of high quality simulations would have to be carried out to determine the critical value e.g., Gilpin et al. [17] went through this exercise experimentally for the plate case.

Since, the onset of instability was not predicted well in the case of the flat plate even with a DNS, this exercise could not be attempted properly.

Overall, determination of a thermal instability parameter and criteria for this configuration would be a valuable contribution. It will be a part of future investigation.

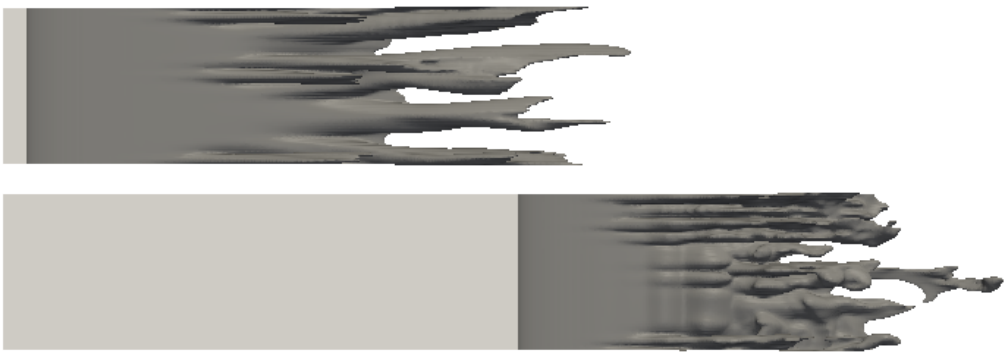

Figure 5.3: $T = 320$ [K] iso-surfaces: $L_{upstream}$ equal to 0.05 [m] (top) and equal to 1 [m] (bottom). Upstream BL development length is shown in light gray.

5.3 Effect of incoming BL height

Two simulations were carried out with $L_{upstream}$ set to values of 0.05 and 1 [m] in order to understand the effects of incoming BL height. L_{strip} used in these simulations was the same and had a value of 0.05 [m].

Temperature iso-surfaces, contours, plots from 2D FFT at different planes and streamwise evolution of different terms in the vorticity equation are presented in Figures 5.3 to 5.7. In Figures 5.4 and 5.6 the planes have been chosen such that they have the same location relative to the strip. For instance, in the first (second) case the strip starts at $x = 0.05$ ($x = 1$) [m], has a length of 0.05 (0.05) [m] and the location chosen for the first plane is $x = 0.7$ ($x = 1.65$) [m] which is 0.6 [m] downstream of the strip edge in both the cases. The intent was to quantify the differences due to the incoming BL height.

Before discussing the effects of the upstream BL development length on flow structures, it is of interest to compare Figure 4.7 (bottom) with Figure 5.3 (top),

where the former is a hot plate at $T = 1500$ [K] and the latter is a hot strip at the same temperature with a fairly small upstream BL development length. Clearly, the length scale keeps on increasing in the former setup whereas the largest scale in the latter case seems to be limited by the length of the strip (since that is the major difference between the two configurations). So, one should expect the flame towers observed e.g., by Gorham [1] to be connected to the streamwise length of the burner.

In the experiments with stationary burners by Gorham [1] it was shown that a longer $L_{upstream}$ leads to more thin horizontal structures, which is exactly what can be observed in Figure 5.3 as well, thus giving confidence in the chosen non-reacting configuration, which does not involve any combustion/radiation modelling related issues.

Some comments can be made based on Figures 5.4 and 5.6 e.g., in the latter case the the dominant modes are relatively smaller (larger) in the wavenumber (physical) space, which is what was expected as in the latter case buoyancy gets more important since the free stream flow has bigger BL and hence has less momentum. Due to a relatively more dominant buoyancy force the structures in Figure 5.6 have also reached a higher altitude.

Also streamwise evolution of various terms in the streamwise vorticity equation happens relatively quickly (after the edge of the strip) in the latter case.

But it is clear that unless the metric contains information accumulated over a certain duration (currently only one snapshot is being analyzed) nothing concrete can be said (because every snapshot will have structures slightly different from the

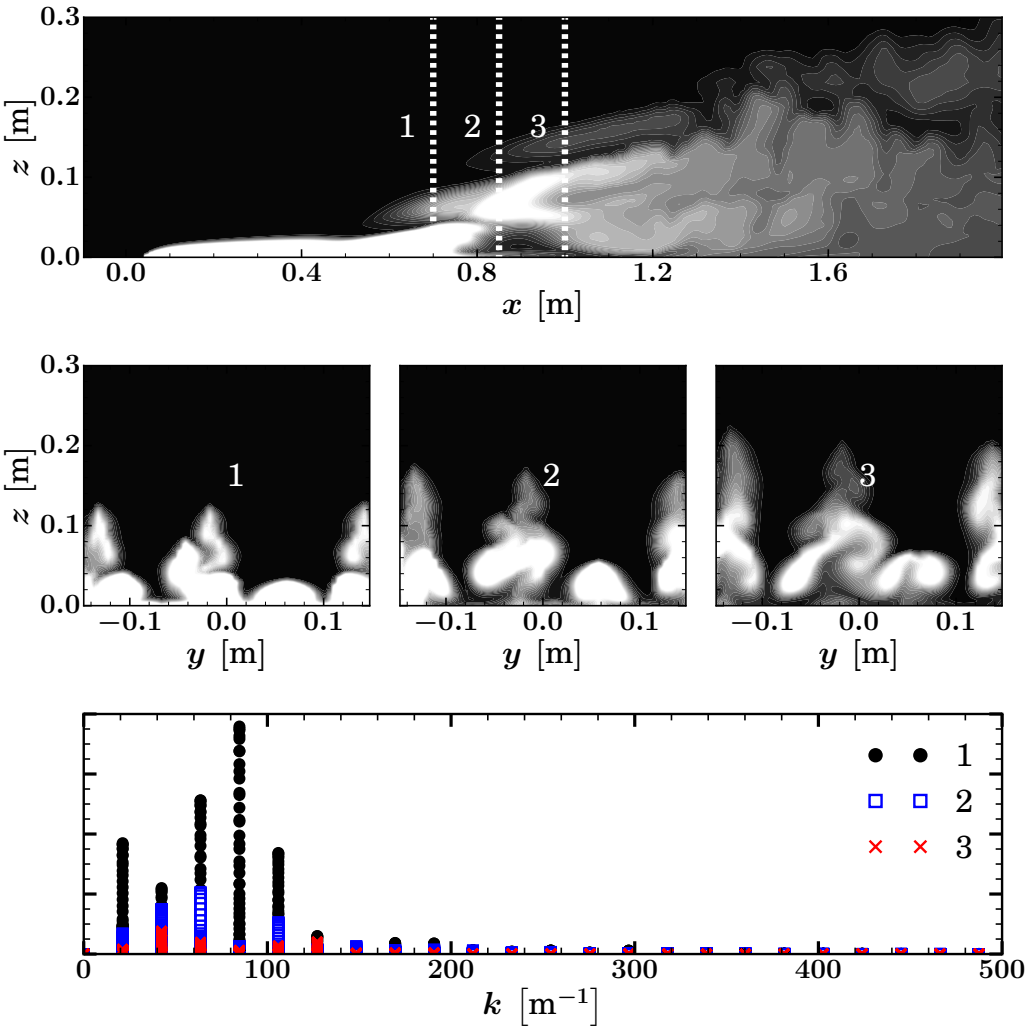

Figure 5.4: Flow over a hot isothermal strip (at $T = 1500$ [K]) of length 5 [cm] with upstream BL development length of 5 [cm]: Contours of temperature; at plane $y = 0$ [m] (top), at planes $x = 0.7$, $x = 0.85$ and $x = 1.0$ [m] (middle, from left to right) and two dimensional fourier transform of T at planes $x = 0.7$, $x = 0.85$ and $x = 1.0$ [m] (bottom). For the contours white (black) corresponds to $T > 320$ ($T = 300$) [K].

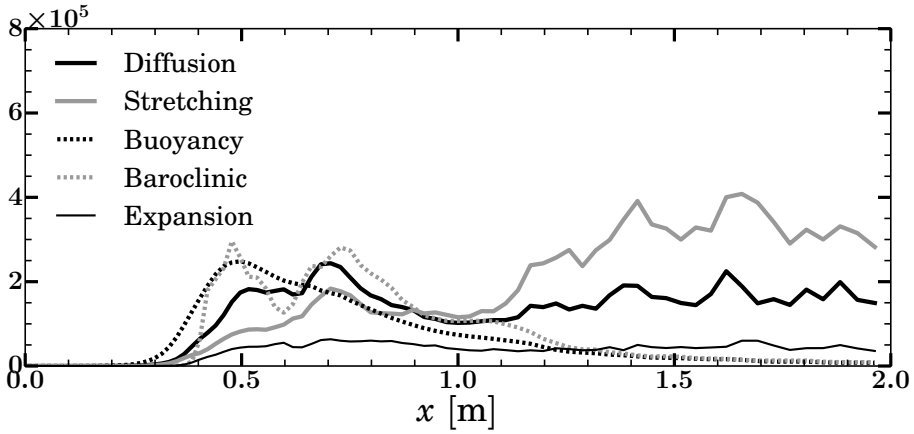

Figure 5.5: Flow over a hot isothermal hot strip of length 0.05 [m], at 1500 [K], with an upstream BL development of 0.05 [m]: Variation of different terms, in the streamwise vorticity equation, along the length of the plate.

other snapshot) e.g., about how the incoming BL height affects the size of the larger structures. This comment also applies to the flat plate simulations.

In this direction, a literature survey was conducted and two techniques were identified Proper Orthogonal Decomposition (POD) [72] and Dynamic Mode Decomposition (DMD) [73]. The former method determines the most energetic structures by diagonalizing the spatial correlation matrix computed from the snapshots. But one of the drawbacks of this method is that the energy may not in all circumstances be the correct measure to rank the flow structures (which is where the latter method will be useful). Note that it is capable of extracting information from snapshots of the flow field and is thus also applicable to experimental data.

The latter method (which has attracted a lot of attention recently) analyzes empirical data, typically generated by nonlinear dynamics, and computes eigenvalues and eigenmodes of an approximate linear model. Without explicit knowledge of the

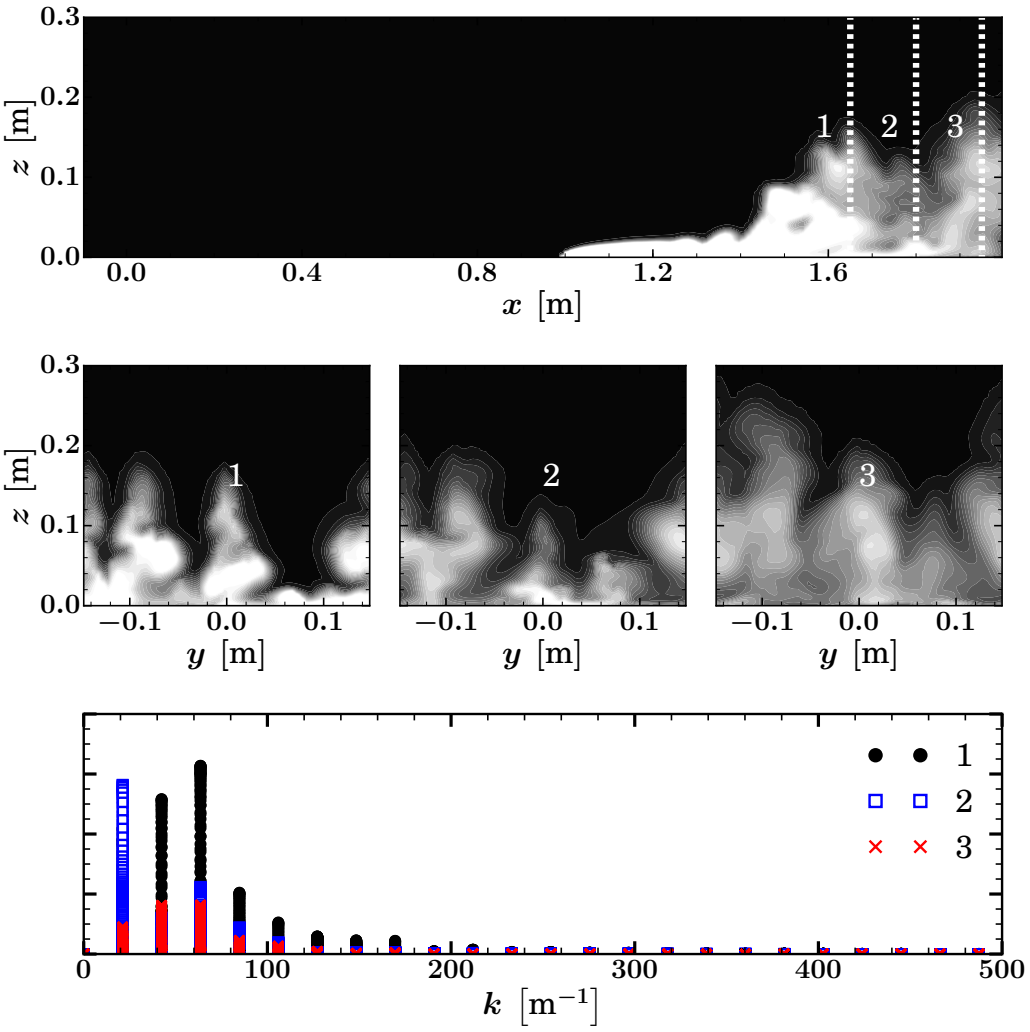

Figure 5.6: Flow over a hot isothermal strip (at $T = 1500$ [K]) of length 5 [cm] with upstream BL development length of 100 [cm]: Contours of temperature; at plane $y = 0$ [m] (top), at planes $x = 1.65$, $x = 1.8$ and $x = 1.95$ [m] (middle, from left to right) and two dimensional fourier transform of T at planes $x = 1.65$, $x = 1.8$ and $x = 1.95$ [m] (bottom). For the contours white (black) corresponds to $T > 320$ ($T = 300$) [K].

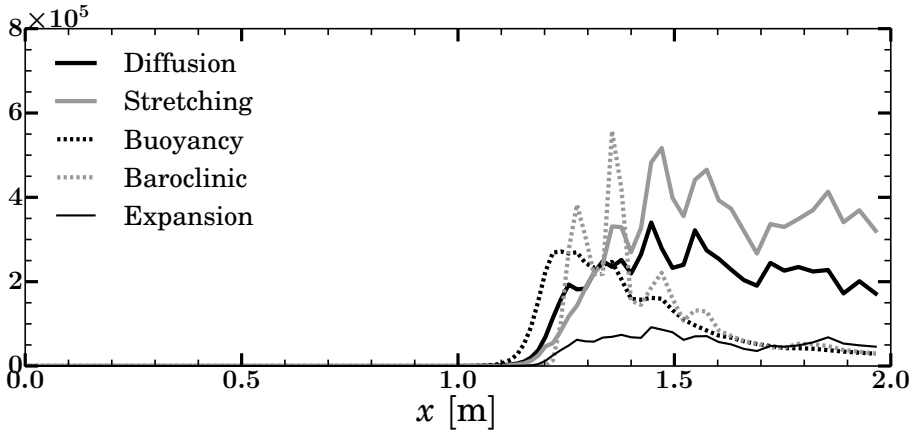

Figure 5.7: Flow over a hot isothermal hot strip of length 0.05 [m], at 1500 [K], with an upstream BL development of 1.0 [m]: Variation of different terms, in the streamwise vorticity equation, along the length of the plate.

dynamical operator, it extracts frequencies, growth rates, and spatial structures for each mode. Consequently, it is expected to provide quality insight into the flow structures seen in the present configuraton and also in the hot plate configuration (Chapter 4). This method can also handle experimental databases.

Both these techniques will be explored, to quantify the effects of the incoming BL height on the larger structures, in the future.

5.4 Effect of streamwise length of the strip

Another simulation was undertaken where the strip length used was 0.5 [m]. $L_{upstream}$ was kept equal to 0.05 [m] in order to have enough downstream domain length for the development of the flow. The results can be seen in Figures 5.8 to 5.10. Again the planes have been placed such that they are at the same downstream location relative to the strip, similar to what was done for the previous two

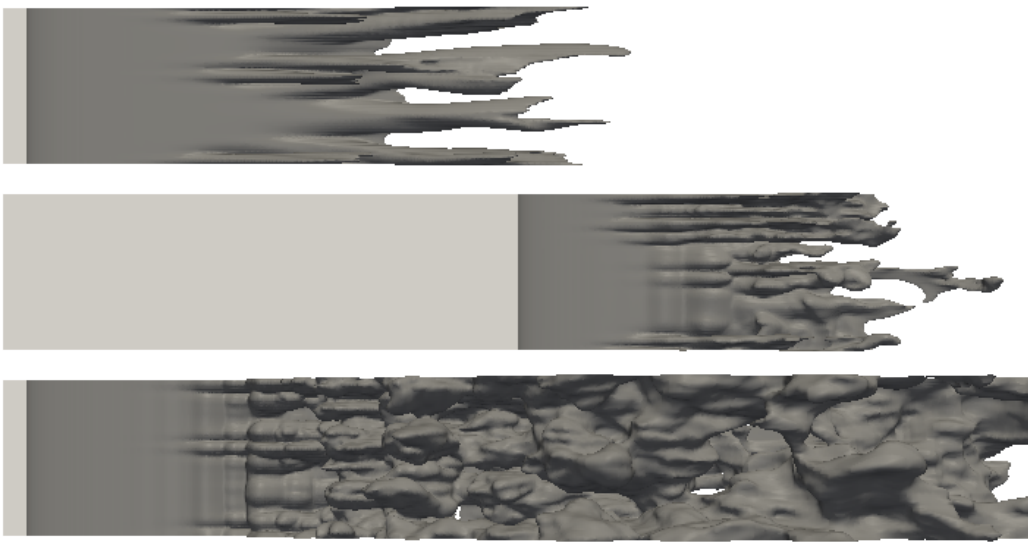

Figure 5.8: $T = 320$ [K] iso-surfaces: $L_{upstream}$ (L_{strip}) equal to 0.05 (0.05) [m] (top), 1 (0.05) [m] (middle) and 0.05 (0.5) [m] (bottom). Upstream BL development length is shown in light gray.

simulations.

From Figures 4.7 and 5.8 it is clear that the length scale of (or spacing between) the thin horizontal structures is fairly insensitive to changes in e.g., the plate temperature, the upstream BL development length and the length of the hot strip. Which, as already mentioned, seems analogous to the insensitivity of the MDM to various parameters (due to the cube root), Equation 3.4, given by LSTV for RTI.

However, the number of these structures is certainly very sensitive e.g., to the upstream BL development length (due to a relatively lower momentum in the cross flow); also shown by Gorham [1] in his stationary burner experiments.

As expected (since we have a stronger presence of buoyancy in this case due to an increased length of the strip) the modes identified in this case are smaller (larger)

in the wavenumber (physical) space than those seen in the case with $L_{strip} = 0.05$ [m]. From the peaks given by 2D FFT of plane 1 (black symbols) in Figures 5.4 and 5.9 one can say that the length scale in the case with a longer (0.5 [m] in length) strip ($2\pi/40 = 0.16$ [m]) is twice that ($2\pi/80 = 0.08$ [m]) seen with the shorter strip (0.05 [m] in length).

But the comparisons change from plane to plane at this point since the diagnosis is based on a single snapshot of the flow field, which is where techniques like POD and DMD will help.

It was also interesting to compare the results from this case with the plate case in which temperature of the plate was 1500 [K]. In order to make a clear comparison the contour range is adjusted, i.e., $T > 500$ ($T = 300$) [K] is colored white (black), see Figure 5.11 for an updated presentation. The plane locations are also changed to match those used in Figure 4.8. It can be observed that at plane three this case does not provide us any structures (contrary to the plate case with the same temperature) since the effects of buoyancy are almost lost by that point in space. As already mentioned, this is precisely the reason why flame towers observed e.g. in [1] are expected to depend upon the streamwise length of strip.

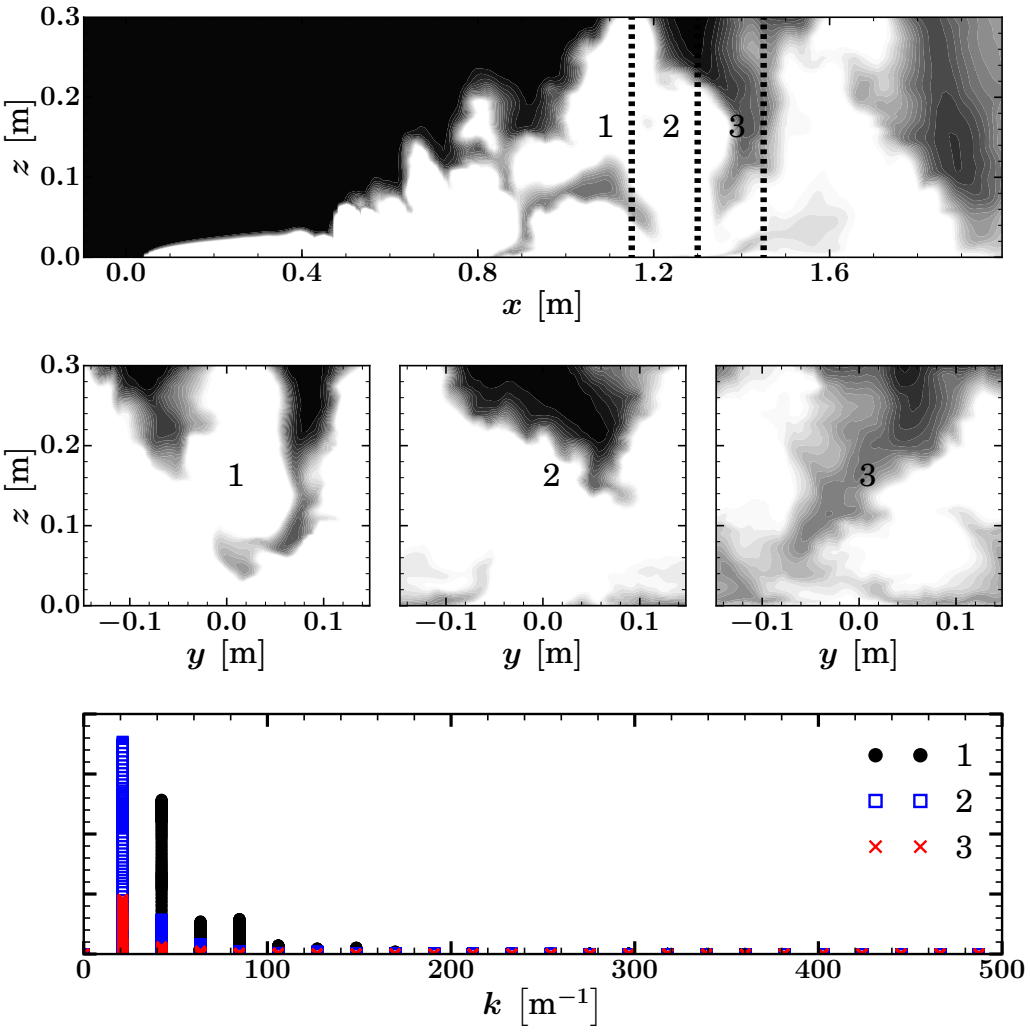

Figure 5.9: Flow over a hot isothermal strip (at $T = 1500$ [K]) of length 50 [cm] with upstream BL development length of 5 [cm]: Contours of temperature; at plane $y = 0$ [m] (top), at planes $x = 1.15$, $x = 1.3$ and $x = 1.45$ [m] (middle, from left to right) and two dimensional fourier transform of T at planes $x = 1.15$, $x = 1.3$ and $x = 1.45$ [m] (bottom). For the contours white (black) corresponds to $T > 320$ ($T = 300$) [K].

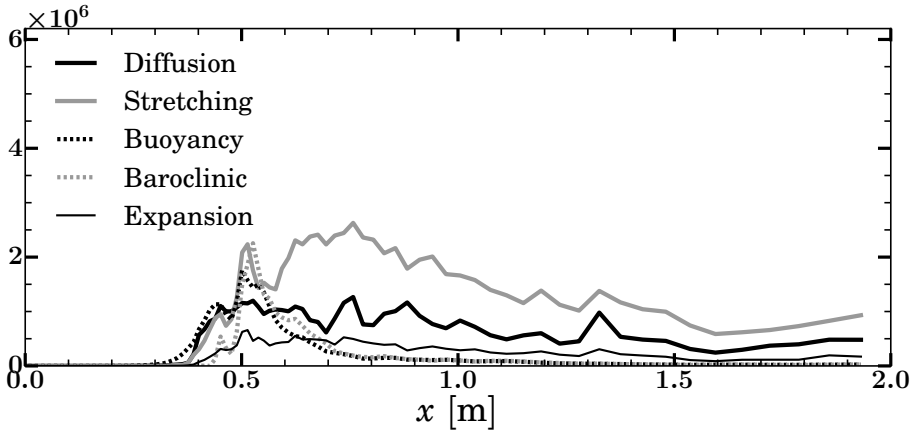

Figure 5.10: Flow over a hot isothermal hot strip of length 0.5 [m], at 1500 [K], with an upstream BL development of 0.05 [m]: Variation of different terms, in the streamwise vorticity equation, along the length of the plate.

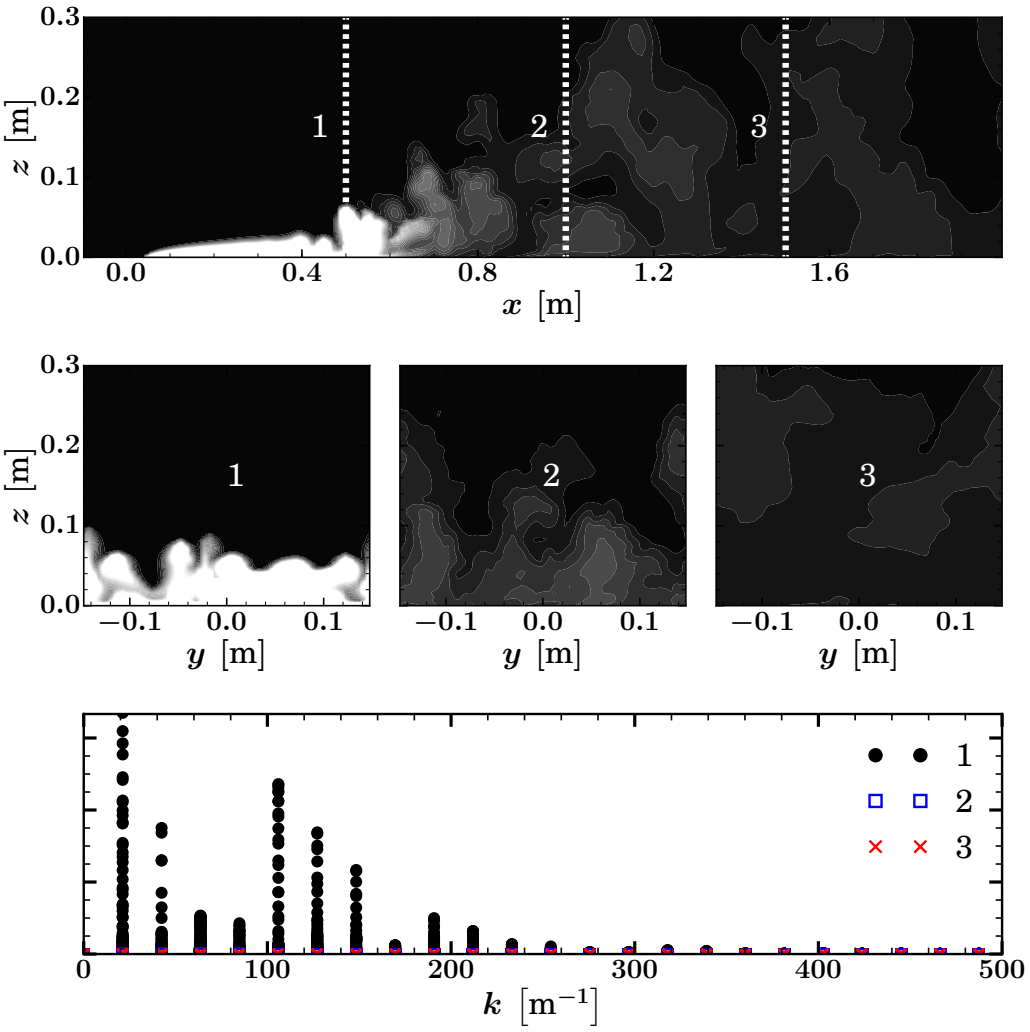

Figure 5.11: Flow over a hot isothermal strip (at $T = 1500$ [K]) of length 50 [cm] with upstream BL development length of 5 [cm]: Contours of temperature; at plane $y = 0$ [m] (top), at planes $x = 0.5$, $x = 1.0$ and $x = 1.5$ [m] (middle, from left to right) and two dimensional fourier transform of T at planes $x = 0.5$, $x = 1.0$ and $x = 1.5$ [m] (bottom). For the contours white (black) corresponds to $T > 500$ ($T = 300$) [K].

6: Summary, conclusions and future work

6.1 Summary

- FireFOAM has been thoroughly verified/validated against Linear Stability Theory for Rayleigh-Taylor Instability, both in terms of the exponential perturbation growth and the Most Dangerous Mode.

- Different stages of Rayleigh-Taylor Instability, have been simulated. It temporally takes the same course as the streaks take spatially in e.g. the stationary burners [1].

- First Direct Numerical Simulation for predicting the onset of thermal instability in Configuration 2 has been carried out.

- Spatial evolution of various terms in the streamwise vorticity equation has been analyzed to identify the dominant contributors towards the generation/evolution of streamwise vorticity in Configuration 2.

- Streamwise evolution of the thermal instability in Configuration 2 has been qualitatively shown. Simulations suggest that flow fluctuations follow a natural evolution from high- to low-frequency/wavenumber (corresponding length scales grow in size) as one moves to downstream locations. There is no natural limit to that evolution in Configuration 2.

- Effects of changes in the temperature and orientation of the plate on the instabilities have been qualitatively shown.

- In Configuration 3; the effects of changes in the upstream Boundary Layer height and the streamwise length of the hot strip have been shown, again qualitatively. Simulations suggest that flow fluctuations follow again a natural evolution from high- to low-frequency/wavenumber (corresponding length scales grow in size) as one moves to downstream locations. There is now a natural limit to that evolution associated with the size of the strip.

6.2 Conclusions

As already pointed out, lack of a quality diagnostic tool (like Proper Orthogonal Decomposition and Dynamic Mode Decomposition) did not allow us to draw too many quantitative conclusions. But the following can be said -

- FireFOAM has been shown to be a powerful tool for analyzing thermal instabilities.

- In Configuration 2, buoyancy has been shown to be the single most important term in the streamwise vorticity equation.

- In Configuration 2 length scales keep on increasing as one moves to downstream locations.

- A larger incoming Boundary Layer height (or a longer streamwise length of the strip) in Configuration 3 leads to larger structures due a relatively larger strength of buoyancy.

- The Flame Tower like structures, not surprisingly are connected to the stream-wise length of the strip in Configuration 3.

6.3 Future work

- Sub-Grid Scale turbulence modelling strategy will be re-visited. In particular Burton's Non-linear Large Eddy Simulation (nLES) looks very promising and will be implemented and tested.

- The discrepancy between Direct Numerical Simulations (DNS) and Gilpin et al.'s [17] criterion for thermal instability onset Configuration 2 will be investigated.

- Dynamic Mode Decomposition (DMD) [73] will be implemented inside the OpenFOAM framework. Proper Orthogonal Decomposition (POD) [72] is already available but will be thoroughly tested.

- Utilizing Proper Orthogonal and Dynamic Mode Decomposition, evolution of the structures/instabilities in Configuration 2 will be studied.

- Critical parameter for thermal instability in Configuration 3 will be determined.

- The critical thermal instability onset value of the critical parameter for Configuration 3 will be determined using Direct Numerical Simulations. Essentially this exercise (and the one above) will include the effects of incoming Boundary Layer height which were recently investigated, experimentally, by Gorham [1]

for stationary burners.

- Correlation between the streamwise length of the strip and the largest observed structures (or Flame Tower like structures) will be established in Configuration 3.

- Finally, stationary burner experiments [1] will be simulated and the results (e.g., the spacing between the longitudinal vortices and the Flame Towers) will be compared with the experimental data.

Bibliography

[1] D. Gorham. Studying wildland fire spread using stationary burners. Master's thesis, University of Maryland, College Park, USA, 2014.

[2] M.A Finney, J.D. Cohen, S.S. McAllister, and M.W. Jolly. On the need for a theory of wildland fire spread. *International journal of wildland fire*, 22:25–36, 2013.

[3] R.C. Rothermel. A mathematical model for predicting fire spread in wildland fuels. *USDA Forest Service, Intermountain Forest and Range Experiment Station*, INT:115, 1972.

[4] M.A. Finney, J. Forthofer, I.C. Grenfell, B.A. Adam, N.K. Akafuah, and K. Saito. A study of flame spread in engineered cardboard fuelbeds: Part I: Correlations and observations. *Seventh International Symposium on Scale Modeling (ISSM-7)*, 2013.

[5] D.A. Haines. Horizontal roll vortices and crown fires. *Journal of Applied Meteorology*, 21:751–763, 1982.

[6] D.A. Haines and M.C. Smith. Three types of horizontal vortices observed in wildland mass and crown fires. *Journal of Climate and Applied Meteorology*, 26:1624–1637, 1987.

[7] H. Imura, R.R. Gilpin, and K.C Cheng. An experimental investigation of heat transfer and buoyancy induced transition from laminar forced convection to turbulent free convection over a horizontal isothermally heated plate. *Journal of Heat Transfer*, 100:429–434, 1978.

[8] M.A. Finney, J. Forthofer, I.C. Grenfell, B.A. Adam, N.K. Akafuah, and K. Saito. A study of flame spread in engineered cardboard fuelbeds: Part II: Scaling law approach. *Seventh International Symposium on Scale Modeling (ISSM-7)*, 2013.

[9] D.J. Gorham, R. Hakes, A.V. Singh, J. Forthofer, S.S. McAllister, M.A. Finney, and M.J. Gollner. Studying Wildland Fire Spread Using Stationary Fires . *VII International Conference on Forest Fire Research*, 2014.

[10] Y. Mori. Buoyancy effects in forced laminar convection flow over a horizontal flat plate. *Journal of Heat Transfer*, 83C:479–482, 1961.

[11] E.M. Sparrow and W.J. Minkowycz. Buoyancy effects on horizontal boundary layer Row and heat transfer. *International Journal of Heat and Mass Transfer*, 5:501–511, 1962.

[12] E.G. Hauptmann. Laminar boundary-layer flows with small buoyancy effects. *International Journal of Heat and Mass Transfer*, 8:289–295, 1965.

[13] I.G. Redekopp and A.F Charwat. Role of Buoyancy and the Boussinesq approximation in horizontal boundary layers. *Journal of Hydronautics*, 6:34–39, 1972.

[14] R.S. Wu and K.C Cheng. Thermal instability of Blasius flow along horizontal plates. *International Journal of Heat and Mass Transfer*, 19:907–912, 1976.

[15] T.S. Chen and A. Mucoglu. Wave instability of mixed convection flow over a horizontal flat plate. *International Journal of Heat and Mass Transfer*, 22:185–196, 1979.

[16] A. Moutsoglou, T.S. Chen, and K.C. Cheng. Vortex instability of mixed convection flow over a horizontal flat plate. *Journal of Heat Transfer*, 103:257–261, 1981.

[17] R.R. Gilpin, H. Imura, and K.C Cheng. Experiments on the onset of longitudinal vortices in horizontal Blasius flow heated from below. *Journal of Heat Transfer*, 100:71–77, 1978.

[18] J.Y. Yoo, P. Park, C.K. Choi, and S.T. Ro. An analysis on the thermal instability of forced convection flow over isothermal horizontal flat plate . *International Journal of Heat and Mass Transfer*, 30:927–935, 1987.

[19] G.J. Hwang and M.H. Lin. Estimation of the onset of longitudinal vortices in a laminar boundary layer heated from below . *Journal of Heat Transfer*, 117:835–842, 1995.

[20] T.K. Sengupta and K. Venkata Subbaiah. Spatial Stability for Mixed Convection Boundary Layer over a Heated Horizontal Plate . *Studies in Applied Mathematics*, 117:265–298, 2006.

[21] T.K. Sengupta, S. Unnikrishnan, S. Bhaumik, P. Singh, and S. Usman. Linear Spatial Stability Analysis of Mixed Convection Boundary Layer over a Heated Plate . *Progress in Applied Mathematics*, 1:71–89, 2011.

[22] X.A. Wang. An Experimental Study of Mixed, Forced, and Free Convection Heat Transfer From a Horizontal Flat Plate to Air. *Journal of Heat Transfer*, 104:139–144, 1982.

[23] S.S. Moharreri, B.F. Armaly, and T.S. Chen. Measurements in the Transition Vortex Flow Regime of Mixed Convection Above a Horizontal Heated Plate. *Journal of Heat Transfer*, 110:358–365, 1988.

[24] K.C. Cheng, T. Obata, and R.R. Gilpin. Buoyancy Effects on Forced Convection Heat Transfer in the Transition Regime of a Horizontal Boundary Layer Heated From Below. *Journal of Heat Transfer*, 110:596–603, 1988.

[25] K.C. Cheng and Y.W. Kim. Flow Visualization Studies on Vortex Instability of Natural Convection Flow Over Horizontal and Slightly Inclined Constant-Temperature Plates. *Journal of Heat Transfer*, 110:608–615, 1986.

[26] N. Ramachandran, B. Armaly, and T. Chen. Turbulent Mixed Convection Over an Isothermal Horizontal Flat Plate. *Journal of Heat Transfer*, 112:124–129, 1990.

[27] A. Ojofeitimi. *On The Computation Of Buoyancy Affected Turbulent Wall Flows Using Large Eddy Simulation*. PhD thesis, University of Maryland, College Park, US, 2013.

[28] D.A. Haines and M.C. Smith. Wind tunnel generation of horizontal roll vortices over a differentially heated surface. *Nature*, 306:351–352, 1983.

[29] M.C. Smith, D.A. Haines, and W.A. Main. Some characteristics of longitudinal vortices produced by line-source heating in a low-speed wind tunnel . *International Journal of Heat and Mass Transfer*, 29:59–68, 1986.

[30] W.E. Heilman and J.D. Fast. Simulations of horizontal roll vortex development above lines of extreme surface heat- ing. *International Journal of Wildland Fire*, 2:55–68, 1992.

[31] W.E. Heilman. Atmospheric simulations of extreme surface heating episodes on simple hills. *International Journal of Wildland Fire*, 299:1–14, 1992.

[32] FM Global. FireFOAM. Available from: https://code.google.com/p/firefoam-dev/.

[33] Y. Wang, P. Chatterjee, and J.L. de Ris. Large eddy simulation of fire plumes. *Proceedings of the Combustion Institute*, 33:2473–2480, 2011.

[34] OpenCFD Ltd. OpenFOAM. Available from: http://www.openfoam.com/.

[35] H.G. Weller, G. Tabor, H. Jasak, and C. Fureby. A tensorial approach to computational continuum mechanics using object-oriented techniques. *Computers in Physics*, 12:620–631, 1998.

[36] T. Poinsot and D. Veynante. *Theoretical and Numerical Combustion*. R.T. Edwards Inc., 2001.

[37] M. Chaos, M.M. Khan, and S.B. Dorofeev. Pyrolysis of corrugated cardboard in inert and oxidative environments. *Proceedings of the Combustion Institute*, 34:2583–2590, 2013.

[38] P. Chatterjee, J.L. de Ris, Y. Wang, and K.B. Dorofeev. A model for soot radiation in buoyant diffusion flames. *Proceedings of the Combustion Institute*, 33:2665–2671, 2011.

[39] K.V. Meredith, J. de Vries, Y. Xin, and Y. Wang. A comprehensive model for simulating the interaction of water with solid surfaces in fire suppression environments. *Proceedings of the Combustion Institute*, 34:2719–2726, 2013.

[40] P. Moin and K. Mahesh. Direct numerical simulation: a tool in turbulence research. *Annual Review of Fluid Mechanics*, 30:539–578, 1998.

[41] C. Meneveau and J. Katz. Scale invariance and turbulence models for large-eddy simulation. *Annual Review of Fluid Mechanics*, 32:1–32, 2000.

[42] D.C. Wilcox. *Turbulence Modeling for CFD*. DCW Industries Inc., 1993.

[43] H. Jasak. *Error Analysis and Estimation for the Finite Volume Method with Applications to Fluid Flows*. PhD thesis, Imperial College, London, UK, 1996.

[44] F.F. Grinstein, L.G. Margolin, and W.J. Rider. *Implicit Large Eddy Simulation: Computing Turbulent Fluid Dynamics*. Cambridge University Press, 2011.

[45] M. Shur, P. Spalart, M. Strelets, and A. Travin. Towards the Prediction of Noise from Jet Engines. *International Journal of Heat and Fluid Flow*, 24:551–561, 2003.

[46] L. Rayleigh. Investigation of the character of the equilibrium of an incompressible heavy fluid of variable density. *Proceedings of the Royal Mathematical Soceity*, 14:170–177, 1883.

[47] G.I. Taylor. The Instability of liquid surfaces when accelerated in a direction perpendicular to their planes. *Proceedings of the Royal Soceity, London*, A201:159–74, 1950.

[48] G. Bateman. *MHD Instabilities*. MIT Press, 1979.

[49] R.D. Petrasso. Rayleigh's challenge endures. *Nature*, 367:217–218, 1994.

[50] R.P. Taleyarkhan, C.D. West, J.S. Cho, R.T. Lahey Jr., R.I. Nigmatulin, and R.C. Block. Evidence for nuclear emissions during acoustic cavitation. *Science*, 295:1868–1873, 2002.

[51] W.H. Cabot and A.W. Cook. Reynolds number effects on Rayleigh-Taylor instability with possible implications for type-Ia supernovae. *Nature Physics*, 2:562–568, 2006.

[52] V.N. Gamezo, Khokhlov A.M., and Oran E.S. Three-dimensional Delayed-Detonation Model of Type Ia Supernovae. *The Astrophysical Journal*, 623:337–346, 2005.

[53] D.H. Sharp. An overview of Rayleigh-Taylor instability. *Physica D: Nonlinear Phenomena*, 12:3–10, 1984.

[54] G. Tryggvason. Numerical Simulations of the Rayleigh-Taylor Instability. *Journal of Computational Physics*, 75:253–282, 1988.

[55] S.I. Abarzhi. Review of theoretical modelling approaches of Rayleigh-Taylor instabilities and turbulent mixing. *Philosophical Transactions of the Royal Society A*, 368:1809–1828, 2010.

[56] T. Wei and D. Livescu. Late-time quadratic growth in single-mode Rayleigh-Taylor instability. *Physical Review E*, 86:046405, 2012.

[57] S. Chandrasekhar. The character of the equilibrium of an incompressible heavy viscous fluid of variable density. *Mathematical Proceedings of the Cambridge Philosophical Society*, 51:162–178, 1955.

[58] R.E. Duff, Harlow F.H., and Hirt C. Effects of diffusion on interface instability between gases. *Physics of Fluids*, 5:417–425, 1962.

[59] S. Gauthier and B. Le Creurer. Compressibility effects in Rayleigh-Taylor instability-induced flows . *Philosophical Transactions of the Royal Society A*, 368:1681–1704, 2010.

[60] A.W. Cook and P.E. Dimotakis. Transition stages of Rayleigh-Taylor instability between miscible fluids. *Journal of Fluid Mechanics*, 443:69–99, 2001.

[61] A.W. Cook, W. Cabot, and P.L. Miller. The mixing transition in Rayleigh-Taylor instability. *Journal of Fluid Mechanics*, 511:333–362, 2004.

[62] E. Fournier, S. Gauthier, and F. Renaud. 2D pseudo-spectral parallel Navier-Stokes simulations of compressible Rayleigh-Taylor instability . *Computers & Fluids*, 31:569–587, 2002.

[63] D. Livescu. Compressibility effects on the Rayleigh-Taylor instability growth between immiscible fluids . *Physics of Fluids*, 16:118–127, 2004.

[64] N.N. Anuchina, V.I. Volkov, V.A. Gordeychuk, Eskov N.S, O.S. Ilyutina, and O.M. Kozyrev. Numerical simulations of Rayleigh-Taylor and Richtmyer-Meshkov instability using MAH-3 code . *Journal of Computational and Applied Mathematics*, 168:11–20, 2004.

[65] G. Burton. Study of ultrahigh Atwood-number RayleighTaylor mixing dynamics using the nonlinear large-eddy simulation method . *Physics of Fluids*, 23:045106, 2011.

[66] G.C. Burton. Large-eddy simulation of ultra-high Atwood number Rayleigh-Taylor mixing using the nLES method . *Annular Research Briefs, Center for Turbulence Research, Stanford University*, 2009.

[67] G. Blanquart and H Pitsch. Large-eddy simulation of a turbulent buoyant helium plume . *Annular Research Briefs, Center for Turbulence Research, Stanford University*, 2008.

[68] D.L. Youngs. Three-dimensional numerical simulation of turbulent mixing by Rayleigh-Taylor instability. *Physics of Fluids*, 3:1312, 1991.

[69] D.L. Youngs. Application of monotone integrated large eddy simulation to Rayleigh-Taylor mixing. *Philosophical Transactions of the Royal Society A*, 367:2971, 2009.

[70] J.M. Forthofer and S.L. Goodrick. Review of Vortices in Wildland Fire . *Journal of Combustion*, 2011:1–14, 2011.

[71] G.I. Taylor, A.E. Green, M. Strelets, and A. Travin. Mechanism of the production of small eddies from large ones. *Proceedings of the Royal Society of London A*, 158:499–521, 2002.

[72] P. Holmes, J.L. Lumley, G. Berkooz, and C.W. Rowley. *Turbulence, Coherent Structures, Dynamical Systems and Symmetry*. Cambridge University Press, 2012.

[73] P.J. Schmid. Dynamic mode decomposition of numerical and experimental data. *Journal of Fluid Mechanics*, 656:5–28, 2010.